

Microbial uptake in oral mucosa-draining lymph nodes leads to rapid release of cytotoxic CD8⁺ T cells lacking a gut-homing phenotype.

Barreto de Albuquerque J, Altenburger LM, Abe J, von Werdt D, Wissmann S, Martínez Magdaleno J, Francisco D, van Geest G, Ficht X, Iannacone M, Bruggmann R, Mueller C, Stein JV. *Sci Immunol*. 2022 Jun 24;7(72):eabf1861. doi: 10.1126/sciimmunol.abf1861. Epub 2022 Jun 17. PMID: 35714202

1 **Microbial uptake in oral mucosa-draining lymph nodes leads to rapid release of**
2 **cytotoxic CD8⁺ T cells lacking a gut-homing phenotype**

3

4 Juliana Barreto de Albuquerque^{1,*}, Lukas M. Altenburger^{2,#}, Jun Abe^{2,#}, Diego von Werdt^{1,#},
5 Stefanie Wissmann², Jose Martínez Magdaleno², David Francisco³, Geert van Geest³, Xenia
6 Ficht^{4,5}, Matteo Iannacone^{4,5,6}, Remy Bruggmann³, Christoph Mueller^{1,*}, Jens V. Stein^{2,*}

7

8 ¹ Division of Experimental Pathology, Institute of Pathology, University of Bern, 3008 Bern,
9 Switzerland

10 ² Department of Oncology, Microbiology and Immunology, University of Fribourg, 1700
11 Fribourg, Switzerland

12 ³ Interfaculty Bioinformatics Unit and Swiss Institute of Bioinformatics, University of Bern,
13 3012 Bern, Switzerland

14 ⁴ Division of Immunology, Transplantation and Infectious Diseases, IRCCS San Raffaele
15 Scientific Institute, Milan, Italy

16 ⁵ Vita-Salute San Raffaele University, Milan, Italy

17 ⁶ Experimental Imaging Center, IRCCS San Raffaele Scientific Institute, Milan, Italy

18

19 # Equal contribution.

20 * Shared corresponding authorship.

21 Lead contact: Jens V. Stein
22 Department of Oncology, Microbiology and Immunology
23 University of Fribourg
24 Ch. du Musée 5
25 CH-1700 Fribourg
26 email: jens.stein@unifr.ch

27

28 **Running title**

29 T cell priming in oral mucosa-draining lymph nodes.

30

31 **Summary**

32 *Listeria monocytogenes* ingestion leads to priming of cytotoxic T cells in oral mucosa-

33 draining mandibular lymph nodes, which contribute to early systemic host protection.

34 **Abstract**

35 The gastrointestinal (GI) tract constitutes an essential barrier against ingested microbes,
36 including potential pathogens. While immune reactions are well-studied in the lower GI tract,
37 it remains unclear how adaptive immune responses are initiated during microbial challenge
38 of the oral mucosa (OM), the primary site of microbial encounter in the upper GI tract. Here,
39 we identify mandibular lymph nodes (mandLN) as sentinel lymphoid organs that intercept
40 ingested *Listeria monocytogenes* (Lm). Oral Lm uptake led to local activation and release of
41 antigen-specific CD8⁺ T cells that constituted the majority of the early circulating effector T
42 cell (T_{EFF}) pool. MandLN-primed T_{EFF} disseminated to lymphoid organs, lung and OM, and
43 contributed substantially to rapid elimination of target cells. In contrast to CD8⁺ T_{EFF}
44 generated in mesenteric lymph nodes (MLN) during intragastric infection, mandLN-primed
45 T_{EFF} lacked a gut-seeking phenotype, which correlated with low expression of enzymes
46 required for gut homing imprinting by mandLN stromal and dendritic cells. Accordingly,
47 mandLN-primed T_{EFF} decreased Lm burden in spleen but not MLN after intestinal infection.
48 Our findings extend the concept of regional specialization of immune responses along the
49 length of the GI tract, with CD8⁺ T_{EFF} generated in the upper GI tract displaying homing
50 profiles that differ from those imprinted by lymphoid tissue of the lower GI tract.

51

52 **Introduction**

53 The digestive, or gastrointestinal (GI), tract constitutes the major external surface of the
54 human body and comprises the upper GI tract with oral cavity, pharynx and esophagus, and
55 the lower GI tract with stomach, small and large intestine and rectum. The GI tract needs to
56 offset permissive uptake and digestion of nutrients and water with protection against
57 microbes, including potential pathogens. Accordingly, GI immune responses range from
58 tolerance against commensals and food antigens to reactivity against ingested pathogens.
59 Thus far, innate and adaptive immune responses have been most extensively studied in the
60 lower GI tract (1-6). Gut-associated lymphoid tissues (GALT) of the small intestine such as
61 Peyer's patches (PP), together with gut lymph nodes (gLN), form complementary inductive
62 sites for intestinal immune reactions (7). M cells embedded in the epithelium overlying GALT
63 sample luminal antigen (Ag), while gLN including mesenteric LN (MLN) screen intestinal
64 lymph to intercept pathogens, which have breached the epithelial barrier. Both MLN and PP
65 promote the generation of CD4⁺ and CD8⁺ T effector cells (T_{EFF}) expressing the signature
66 gut-homing receptors $\alpha_4\beta_7$ and CCR9 (8). Induction of a gut-seeking phenotype in activated
67 lymphocytes relies on retinoic acid (RA) synthesis by retinal aldehyde dehydrogenase family
68 1 (Aldh1) family members expressed by CD103⁺ migratory dendritic cells (DC) and stromal
69 cells of intestinal Ag-sampling lymphoid tissue (9-11). Recent findings have further refined
70 our understanding of gut immunity by identifying compartmentalized tolerogenic and
71 inflammatory CD4⁺ T cell immune responses in individual gLN, which drain lymph from
72 proximal versus distal segments of the intestinal GI tract (12, 13). Thus, the intestinal tract is
73 characterized by regional specialization of adaptive immune responses according to the local
74 microenvironment (6).

75 The upper GI tract, in particular the mucosa of the oral cavity, also contains an abundant
76 microbiota and acts as the first site of contact with dietary Ag and ingested microbes,
77 including potential pathogens (14, 15). The oral barrier has recently gained attention for its
78 complex immune network characterized by abundant CD4⁺ T cells and numerous
79 macrophage subsets (14-16). As example, periodontitis, which represents the most common

80 inflammatory disease in humans, is triggered by extracellular bacteria (15). This chronic
81 condition imprints Th17 CD4⁺ T cells with gut-homing capacity, which have recently been
82 linked to inflammatory disorders of the lower GI tract (17). In addition to chronic infection,
83 recent reports have identified the oral cavity as a prominent site of airborne viral replication,
84 including influenza virus and SARS-CoV-2 (18, 19). Similarly, oral ingestion is the most
85 common route of entry for pathogens including *Trypanosoma cruzi* and *Listeria*
86 *monocytogenes* (Lm) causing Chagas disease and listeriosis, respectively (20)
87 (<https://www.who.int/news-room/fact-sheets/detail/listeriosis>). Listeriosis is one of the most
88 serious foodborne diseases and caused by eating contaminated food with high numbers of
89 Lm.

90 Yet, despite the global rise of orally transmitted diseases, the initiation of adaptive immune
91 responses against microbes sampled from oral mucosa (OM) has not been well
92 characterized, in particular for cytotoxic CD8⁺ T cell responses that occur in response to
93 intracellular pathogens. To the best of our knowledge, no comprehensive attempt has been
94 made to map OM-draining LN, although in a rodent periodontitis model, antibacterial
95 responses are detectable in mandibular and accessory mandibular LN (here collectively
96 abbreviated as mandLN; also sometimes referred to as superficial cervical LN) (21-23). Our
97 current understanding of the local immune responses upon oral pathogen exposure is limited
98 since most oral immunization models in small rodents bypass the oral cavity by employing
99 intragastric (i.g.) gavage. In models where pathogens are administered intraorally (i.o.), the
100 analysis of immune responses often excludes lymphoid tissue of the neck and head region
101 (24, 25). Thus, the precise priming location, magnitude and kinetics of oral CD8⁺ T cell
102 responses remain unaddressed to date. Similarly, it remains unclear whether the ensuing
103 T_{EFF} phenotype and dissemination pattern are comparable to the ones observed during
104 intestinal infections and whether local oral cavity-triggered immune reactions impact on
105 immune responses at distal sites (14).

106 Here, we mimicked foodborne listeriosis by Lm administration into the oral cavity of
107 immunocompetent mice or by uptake of Lm-contaminated food. We detected early priming

108 and proliferation of Ag-specific CD8⁺ T cells in mandLN that preceded activation kinetics in
109 spleen, MLN and PP. MandLN-primed CD8⁺ T_{EFF} constituted the majority of early circulating
110 T_{EFF} and disseminated to secondary lymphoid organs (SLO), lung and OM, and contributed
111 to systemic host protection. In contrast to CD8⁺ T_{EFF} primed in MLN after i.g. Lm gavage,
112 mandLN CD8⁺ T_{EFF} did not display a gut-homing phenotype, correlating with low expression
113 of genes imprinting gut homing in the mandLN microenvironment. Our observations expand
114 the emerging concept of a compartmentalized host immune response along the length of the
115 entire GI tract according to the Ag sampling location and identify OM-draining mandLN as a
116 first-line “immunological firewall” after ingestion of microbial pathogens.

117 **Results**

118 *Ingested Lm is intercepted in mandLN and leads to local LN hyperplasia*

119 To examine drainage of OM lymph in C57BL/6 mice, we injected a lymph tracer into gingiva.

120 Within ≤ 5 min after tracer injection, we observed its rapid accumulation in draining mandLN

121 (**Fig. 1A**), suggesting a connecting lymphatic network between oral cavity and mandLN.

122 Based on histological analysis, the gingiva adjacent to teeth was reported to contain

123 numerous lymphatic vessels, which are located more superficially than in most other

124 mucosal tissues (21, 26). To obtain an overview of the intact oral lymphatic network, we

125 carefully exposed the mandibular gingiva and draining mandLN in a Prox1-GFP reporter

126 mouse, which allows the identification of lymphatic vessels (27) (**Fig. S1A**). We confirmed

127 the presence of an extensive gingival lymphatic network around the mandibular incisors (**Fig.**

128 **1B, C**) connected to mandLN (**Fig. 1D**).

129 Next, we investigated the relevance of lymphatic drainage in an oral ingestion model. Lm is a

130 foodborne gram-positive bacterium, which infects macrophages and hepatocytes in its target

131 organs spleen and liver and is cleared by cytotoxic CD8⁺ T_{EFF}. Lm expressing the model

132 antigen ovalbumin (Lm-OVA) (28) was directly administered into the oral cavity of C57BL/6

133 mice. In the first 8 days post i.o. infection, we isolated mandLN, spleen, MLN and PP of

134 infected mice and determined Lm-OVA spread by colony forming unit (CFU) analysis. We

135 compared these values to CFU counts after i.v. administration of Lm-OVA, the most

136 commonly used route for Lm infection in experimental immunology (**Fig. 1E**). We observed

137 that mandLN contained the highest Lm-OVA CFU per organ on d 1 following i.o. infection,

138 whereas spleen contained the highest CFU following systemic administration (**Fig. 1F**). On d

139 3 after i.o. infection, Lm-OVA became also detectable in spleen (**Fig. 1F**). In contrast, Lm-

140 OVA CFU counts in MLN and PP remained low or undetectable in the first week after i.o.

141 infection (**Fig. 1F**). This is in line with the notion that $> 90\%$ of ingested bacteria are killed by

142 gastric acids (29, 30). Residual Lm in the intestinal lumen may have been degraded by

143 digestive enzymes, or failed to cross the mucus layer of the intestinal epithelium or their tight

144 junctions, or become cleared by peristaltic contraction and mucus secretion. Together, these

145 factors likely contribute to the delayed spread of Lm to PP and MLN in our model of oral
146 ingestion.

147 To explore whether high bacterial load correlates with increased lymphocyte numbers in
148 reactive LN, we determined lymphoid organ cellularity following i.v. and i.o. Lm-OVA
149 infection. We observed a rapid onset of mandLN hyperplasia following i.o. infection,
150 consistent with local bacterial sampling at early time points (**Fig. 1G**). In contrast, i.v. Lm-
151 OVA infection did not cause mandLN hyperplasia at any time point analyzed, whereas
152 splenocyte numbers became significantly increased on d 8 p.i. (**Fig. 1G**). In our oral ingestion
153 model, MLN and PP cellularity remained unchanged after Lm infection, consistent with
154 limited CFU detection in the first week p.i. at these sites (**Fig. 1G**).

155 Next, we examined the mechanism underlying microbial sampling of OM by mandLN.
156 Expression of a mutant internalin InIA^m in Lm increases its binding affinity to mouse E-
157 cadherin by four orders of magnitude (31). As a result, i.g. gavage of Lm-InIA^m leads to a
158 higher *in vivo* virulence as compared to non-murinized InIA Lm strains (32). To examine
159 whether the interplay of InIA and E-cadherin facilitates early Lm accumulation in mandLN, we
160 compared CFU counts of Lm-OVA and Lm-InIA^m after i.o. infection. Lm-InIA^m CFU counts in
161 mandLN were significantly increased at 24 h p.i. as compared to Lm-OVA, suggesting that
162 increased adhesion to E-cadherin⁺ OM epithelium might increase transport to mandLN (**Fig.**
163 **1H**). As a caveat, this finding may have been influenced by the higher virulence of the Lm
164 strain carrying the InIA mutation as compared to the Lm-OVA strain (33). To further
165 investigate the mechanism underlying the rapid appearance of ingested Lm in mandLN, we
166 administered i.o. Lm-OVA in CCR7^{-/-} recipients, which lack DC trafficking from peripheral
167 tissues to sentinel LN (34, 35). Bacterial loads in CCR7^{-/-} mandLN on d 1 p.i. were
168 comparable to WT values, suggesting that active DC migration to mandLN was not a limiting
169 factor for initial Lm accumulation in draining LN (**Fig. 1I**).

170 These observations prompted us to examine a passive transport mechanism for ingested Lm
171 via oral cavity-draining lymphatic vessels. We administered GFP-expressing Lm (Lm-GFP)
172 onto the gingiva of mice prepared for intravital imaging to directly explore its retention in

173 draining mandLN. To this end, we adapted a model originally developed for submandibular
174 salivary gland surgery (36) to expose the adjacent mandLN (**Fig. S1B**). Lm-GFP
175 accumulated in the subcapsular sinus (SCS) of mandLN within 120 min post oral deposition,
176 as assessed by two-photon microscopy (2PM)-based intravital imaging of surgically prepared
177 mice (**Fig. 1J**). To assess whether the GFP signal reflects extracellular versus internalized
178 Lm, we treated mandLN single cell suspensions at d 1 post i.o. infection with Lm-OVA or Lm-
179 InIA^m with antibiotics to inhibit growth of extracellular Lm {Jones2015}. These data suggested
180 that most recovered Lm colonies were of extracellular origin (not shown). Taken together, our
181 data suggest that oral uptake of Lm leads to its drainage to mandLN, at least in part via
182 afferent lymphatics of the OM.

183

184 *Ag-specific CD8⁺ T cells form clusters and dynamically interact with CD11c⁺ cells in mandLN*
185 *following i.o. Lm infection*

186 To assess the relevance of Lm capture in mandLN on CD8⁺ T cell activation, we transferred
187 GFP-, dsRed- or tdTom-expressing OT-I TCR tg T cells, which recognize the OVA₂₅₇₋₂₆₄
188 peptide in the context of H-2K^b (37), together with fluorescently labeled polyclonal CD8⁺ T
189 cells into CD11c-YFP mice. In these recipients, CD11c⁺ cells including antigen-presenting
190 DC express YFP (38). One day later, we i.o. infected mice with Lm-OVA and isolated
191 mandLN at 1, 2 and 3 d p.i. for histological analysis (**Fig. 2A**). At 1 d p.i., we observed
192 occasional large clusters of OT-I but not polyclonal CD8⁺ T cells around CD11c⁺ cells in both
193 mandibular and accessory mandibular LN, suggesting early Ag-driven interactions (**Fig. 2B**,
194 left panel). These clusters became smaller on d 2 and 3 post i.o. infection (**Fig. 2B**, middle
195 and right panel). As changes in dynamic T cell behavior act as sensitive indicator for priming
196 and precede detectable expression of activation markers (39, 40), we performed 2PM of
197 mandLN in C57BL/6 or CD11c-YFP recipients containing OT-I T cells and polyclonal control
198 CD8⁺ T cells during the first 72 h post i.o. Lm-OVA infection. To benchmark physiological T
199 cell behavior in steady state, we analyzed naïve OT-I motility parameters in mandLN of
200 uninfected mice. OT-I T cells displayed high speeds ($15.4 \pm 5.1 \mu\text{m}/\text{min}$; mean \pm SD), low

201 arrest coefficients (median of 1.6% of track segments $< 5 \mu\text{m}/\text{min}$; **Fig. 2D, E**) and a
202 corrected track straightness of 8.3 ± 2.7 (median \pm SD, corresponding to a non-corrected
203 meandering index of 0.61 ± 0.21) (41) (**Video S1**). These values are comparable to T cell
204 motility parameters observed in non-inflamed skin-draining LN (42-44), and serve as
205 reference for inflammation-induced changes of dynamic T cell behavior. At d 1 post i.o. Lm
206 infection, polyclonal CD8^+ T cells displayed a random motility pattern comparable to T cell
207 migration in non-inflamed mandLN, albeit with slightly decreased speeds ($12.0 \pm 4.5 \mu\text{m}/\text{min}$)
208 and increased arrest coefficients (**Fig. 2C-E**). This finding is in line with mild motility changes
209 displayed by non-cognate T cells in reactive LN (43). In contrast, many antigen-specific OT-I
210 T cells were found to cluster around CD11c^+ APC on d 1 and 2 p.i. (**Fig. 2C; Video S2**), and
211 most OT-I T cells, in particular in clusters, displayed decreased speeds and high arrest
212 coefficients (**Fig. 2D, E**). Such a behavior is consistent with interaction dynamics driven by
213 high cognate pMHC levels displayed on APC (40, 45). Starting on d 2 post i.o. Lm infection,
214 OT-I T cell speeds and arrest coefficients began to recover, suggesting decreasing Lm-
215 derived Ag presentation (**Fig. 2D, E**). On d 3 post i.o. Lm infection, OT-I cells had dispersed
216 and showed speeds and arrest coefficients largely comparable to polyclonal CD8^+ T cells
217 (**Fig. 2D, E; video S3**). The analysis of the corrected track straightness followed a similar
218 pattern, with OT-I T cells showing transient confinement on d 1 and 2 p.i., which became less
219 apparent on d 3 p.i. (**Fig. 2F**). Taken together, our confocal and dynamic imaging data are
220 consistent with fast and efficient antigen processing in OM-draining mandLN, leading to
221 cognate T cell – APC interactions within the first 2 d post i.o. infection.

222

223 *Oral infection-induced CD8^+ T cell activation in mandLN is mediated by resident and*
224 *migratory DC*

225 Imaging of oral-cavity-draining mandLN suggested local OT-I T cell priming by CD11c^+
226 antigen-presenting DC. We therefore compared the activation status of CD103^- DC, which
227 mostly comprise LN resident cells, and migratory CD103^+ DC in resting and i.o. challenged

228 mandLN on d 1 post i.o. Lm-OVA infection (**Fig. 3A**). Both populations showed higher and/or
229 more frequent expression of CD80 and CD86 as compared to DC isolated from non-infected
230 mandLN, in line with an activated phenotype (**Fig. 3B, C**). We obtained similar results when
231 we analyzed CD80 and CD86 activation markers gating on resident MHCII^{intermediate} CD11c^{high}
232 versus migratory MHCII^{high} CD11c^{intermediate} DC (**Fig. S2A-C**). While d 1 i.o. Lm-OVA-infected
233 LN showed only a minor expansion in total CD11c⁺ MHCII⁺ DC counts (from 15.3 ± 3.4 to
234 $17.1 \pm 3.8 \times 10^4$ cells/LN; mean \pm SD), the percentage and absolute cell numbers of CCR7-
235 expressing CD103⁺ and CD103⁻ cDC1 was significantly increased (from 3.9 ± 1.6 to 7.1 ± 2.0
236 $\times 10^3$ and 1.1 ± 0.2 to $2.4 \pm 1.5 \times 10^3$ cells/LN, respectively; **Fig. S2D**). To further examine
237 whether resident and/or migratory DC were able to activate CD8⁺ T cells, we sorted MHCII⁺
238 CD11c⁺ CD103⁻ and CD103⁺ DC from d 1 i.o. Lm-OVA-infected mandLN. Isolated DC
239 subsets were separately co-cultured *ex vivo* with Cell Tracer Violet (CTV)-loaded OT-I T cells
240 expressing Nur77-GFP as sensitive readouts for proliferation and TCR signaling, respectively
241 (46) (**Fig. 3D**). Both DC subsets induced Nur77-GFP, CD69 and CD25 expression in OT-I T
242 cells, as well as proliferation within 48 h (**Fig. 3E, F**). Thus, while initial Lm accumulation in
243 mandLN occurs in the absence of migratory DC (**Fig. 1I**), these cells contribute to local CD8⁺
244 T cell activation in our experimental model.

245

246 *Oral Lm ingestion-induced mandLN T_{EFF} generation precedes CD8⁺ T cell activation in*
247 *spleen and MLN*

248 We compared our *in vitro* observations with *in vivo* induction of early activation markers
249 CD69 and CD25 on OT-I T cells following i.o. Lm-OVA infection (**Fig. 4A**; for gating strategy
250 see **Fig. S2E**). To exclude potential cross-contamination by interorgan cell trafficking after
251 Lm infection, we performed these experiments in the presence of FTY720, which sequesters
252 T cells in lymphoid tissue. On d 1 post i.o. Lm infection, mandLN OT-I T cells displayed
253 increased levels of CD69, followed by augmented CD25 expression starting on d 2 p.i. (**Fig.**
254 **4B, C**). At this time point, OT-I T cells in spleen and MLN showed a delayed and less

255 pronounced increase in these markers compared to mandLN OT-T cells (**Fig. 4B, C**).

256 Consistent with increased CD25 expression, more than half ($58 \pm 14.7\%$; median \pm SD) of

257 mandLN OT-I T cells had undergone cell proliferation at d 3 post i.o. infection, whereas only

258 $12 \pm 5.3\%$ and $5 \pm 14\%$ of spleen and MLN OT-I T cells had proliferated, respectively (**Fig.**

259 **4D, E**). We observed the same trend on d 4 post i.o. infection (**Fig. 4E**). As a result, OT-I T

260 cell numbers increased almost tenfold in mandLN on d 3 post i.o. infection, whereas i.v.

261 infection induced a delayed and less pronounced expansion of OT-I T cells (**Fig. 4F**).

262 We then characterized general activation markers on T_{EFF} generated following i.o. and i.v. Lm

263 uptake. Irrespective of the route of infection, mandLN T_{EFF} were CD44^{high} CD62L^{low or high} on d

264 5 p.i., whereas spleen T_{EFF} were predominantly CD44^{high} CD62L^{low} (**Fig. 4G, H**). In the

265 memory phase (d 30 p.i.), most OT-I T cells showed a CD44^{high} CD62L^{high} central memory-

266 like phenotype while we detected a minor population of CD44^{high} CD62L^{low} effector memory-

267 like cells in spleen (**Fig. 4H**), again independent of the route of infection. We further

268 examined OT-I differentiation into CD127⁻ KLRG-1⁺ short-lived effector cells (SLEC) and

269 CD127⁺ KLRG-1⁻ memory precursor effector cells (MPEC) after i.o. *versus* i.v. Lm infection

270 (**Fig. 4I**). In both routes of infection, we observed comparable SLEC and MPEC proportions

271 on d 5 p.i. (**Fig. 4H**). At d 30 p.i., KLRG1⁻ CD127⁺ central memory-like T cells prevailed in

272 mandLN and spleen after either infection route (**Fig. 4H**). In sum, our data show that T cell

273 interactions with resident and migratory CD11c⁺ antigen-presenting cells result in T_{EFF}

274 generation in OM-draining mandLN, preceding their activation in other SLO. The similar

275 phenotype of effector and memory T cells irrespective of the route of infection likely reflects

276 the Lm spread by d 3 to 5 p.i. (**Fig. 1F**) and subsequent mixing of activated T cell

277 populations.

278

279 *CD8⁺ T cell activation in mandLN occurs over a wide range of Lm inocula and ingestion of*

280 *Lm-contaminated food*

281 Similar to most published oral infection models, we initially used a large inoculum to induce

282 an adaptive immune response. To test the impact of initial bacterial load on local OT-I T cell

283 activation, we titrated the Lm inoculum and measured OT-I T cell activation and proliferation
284 on d 3 post i.o. infection in the presence of FTY720 (**Fig. S3A**). We observed a dose-
285 dependent effect on total mandLN cellularity and percent CD69⁺ endogenous CD8⁺ T cells,
286 which became less pronounced with decreasing Lm inoculum (**Fig. S3G-I**). This was
287 reflected by a Lm inoculum-dependent activation marker expression and proliferation in OT-I
288 T cells (**Fig. S3B**). Notably, we observed increased expression of CD69 and CD25, as well
289 as proliferation with an inoculum of only 10⁶ Lm (**Fig. S3C-F**). Next, we examined whether
290 OT-I activation is also observed after ingestion of foodborne Lm-OVA. To restrict lymphocyte
291 circulation, we performed these assays in the presence of FTY720 (**Fig. S3J**). Our data
292 confirmed an increase in cellularity and CD69⁺ and CD25⁺ OT-I numbers in mandLN at d 3
293 p.i. (**Fig. S3K-N**). Thus, sufficient antigenic material is collected by sentinel mandLN across
294 four orders of magnitude of initial Lm inoculum and following consumption of contaminated
295 food to trigger local CD8⁺ T_{EFF} generation.

296

297 *MandLN-primed T_{EFF} represent the majority of the early systemic cytotoxic T cell pool*

298 To quantify to which extent mandLN OT-I cells contribute to the early circulating CD8⁺ T_{EFF}
299 pool, we performed i.o. infections in the absence or presence of FTY720 (**Fig. 5A**). FTY720
300 treatment led to a 4.4-fold increase in mandLN OT-I T_{EFF} on d 4 post i.o. Lm infection,
301 corresponding to an increase from 33 ± 3 to 144 ± 30 × 10⁴ cells/LN (mean ± SEM). This
302 increase was mirrored by a concomitant 67% reduction in OT-I T_{EFF} isolated from spleen
303 (from 126 ± 39 to 41 ± 7 × 10⁴ cells in the absence and presence of FTY720, respectively),
304 suggesting that more than 70% of egressed mandLN T_{EFF} relocated to spleen (**Fig. 5B**). On
305 day 5 p.i., we observed a 5-fold increase in mandLN OT-I T_{EFF} (from 26 ± 8 to 127 ± 18 × 10⁴
306 cells/LN) in presence of FTY720 (**Fig. 5B**). This was accompanied by a decrease in splenic
307 OT-I T_{EFF} numbers after FTY720 treatment (499 ± 165 and 209 ± 54 × 10⁴ cells/spleen in
308 absence and presence of FTY720, respectively; **Fig. 5B**) although this did not reach
309 statistical significance. The partial rescue of spleen OT-I numbers on d 5 likely reflects Lm

310 dissemination to spleen by d 3 p.i. and onset of OT-I cell division by d 4 p.i. (**Fig. 1F and Fig.**
311 **4E**). In contrast, MLN OT-I T cell numbers on d 4 or 5 p.i. were not significantly affected by
312 FTY720 treatment (**Fig. 5B**).

313 To directly examine the relocation of mandLN T_{EFF} to other lymphoid organs, we adoptively
314 transferred OT-I T cells expressing the photoconvertible protein Kikume Green-Red (KikGR)
315 (47) one d prior to i.o. Lm-OVA infection. On day 3 p.i., we photoconverted exposed mandLN
316 and isolated mandLN, spleen, MLN, inguinal LN and PP 14 h later for flow cytometry-based
317 detection of activated (CD44^{high}) KikRed⁺ photoconverted OT-I T cells (**Fig. 5C, D**). As
318 predicted, we found most CD44^{high} KikRed⁺ cells in mandLN, reflecting ongoing cell activation
319 (**Fig. 5E**). We recovered the second highest absolute number of photoconverted T_{EFF} in
320 spleen ($1.8 \pm 0.4 \times 10^4$ cells/organ), several times higher than in MLN ($0.6 \pm 0.1 \times 10^4$
321 cells/organ) and other lymphoid organs. Taken together, these data provide direct evidence
322 that CD8⁺ T cell priming in mandLN leads to a rapid release of T_{EFF} into the circulation, with a
323 substantial fraction localizing to spleen.

324 We examined to which extent these early mandLN T_{EFF} contribute to systemic host protection
325 through target cell elimination. To this end, we transferred OT-I T cells into mice that had
326 received an anti-CD62L (L-selectin) mAb 4 h earlier, which selectively blocks T cell entry into
327 peripheral LN (PLN) but only partially affects homing to MLN and PP, while T cell homing to
328 spleen is not impaired (**Fig. 5F**). We confirmed that anti-CD62L mAb treatment resulted in >
329 8-fold decrease in mandLN cellularity that was maintained until d 4 post blockade, while
330 inducing a trend to increased spleen cell numbers and an intermediate reduction on MLN cell
331 numbers (2.2-fold reduction; **Fig. 5G**). In these anti-CD62L mAb-treated recipients, OT-I T
332 cell homing to and priming in mandLN was therefore severely impaired, without affecting
333 CD8⁺ T cell activation in spleen. On d 3 post i.o. Lm-OVA infection, we transferred a 1:1 mix
334 of fluorescently labeled control and OVA₂₅₇₋₂₆₄-pulsed B cells as surrogate target cells and
335 analyzed their ratio in the spleen 12 h post transfer (**Fig. 5H**). Both cell populations were
336 equally recovered from spleens of recipient animals that had not received OT-I T cell and
337 Lm-OVA (ratio OVA₂₅₇₋₂₆₄-pulsed to unpulsed B cells: 0.97 ± 0.05 ; mean \pm SD; **Fig. 5I**). In

338 control mice that had received OT-I T cells and i.o. Lm-OVA without anti-CD62L mAb
339 treatment, most OVA₂₅₇₋₂₆₄-pulsed B cells were eliminated (ratio OVA₂₅₇₋₂₆₄-pulsed compared
340 to unpulsed B cells: 0.04 ± 0.05 ; **Fig. 5I**). In contrast, in anti-CD62L mAb-treated recipients,
341 significantly more OVA₂₅₇₋₂₆₄-pulsed B cells were recovered (ratio OVA₂₅₇₋₂₆₄-pulsed
342 compared to unpulsed B cells: 0.59 ± 0.17 ; **Fig. 5H and I**). This data correlated with strongly
343 reduced OT-I T cell numbers in spleens of anti-CD62L-mAb-treated recipients as compared
344 to control recipients (**Fig. 5J**), which contrasts with the high spleen cellularity in this setting
345 (**Fig. 5G**). Taken together, our data uncover a substantial contribution of T_{EFF} primed in
346 draining mandLN for early containment of an intracellular pathogen, which is reflected by a
347 more than tenfold increase of target cell killing.

348

349 *mandLN T_{EFF} priming does not induce expression of signature gut homing receptors*

350 Recent reports have identified a link between chronic inflammation of the oral cavity and the
351 induction of Th17 CD4⁺ T cells in the draining mandLN that migrate to the intestine and
352 trigger colitis (17, 48). We therefore set out to assess whether T_{EFF} generated in OM-draining
353 mandLN similarly gained the capacity to home and protect against infections of the lower GI
354 tract. To this end, we compared the chemokine and adhesion receptor expression, as well as
355 effector cytokine profile between i.o.-primed mandLN CD8⁺ T_{EFF}, spleen T_{EFF} primed after i.v.
356 (systemic) and MLN T_{EFF} generated by i.g. infection. In addition, we performed subcutaneous
357 (s.c.) Lm infections to compare the OT-I T_{EFF} phenotype after priming in oral cavity-draining
358 mandLN versus skin-draining popliteal LN (popLN) (**Fig. 6A**). Flow cytometry analysis on d 5
359 following i.o., i.v., i.g. and s.c. Lm-OVA infections revealed that irrespective of the route of
360 infection, OT-I T_{EFF} increased expression of the adhesion receptors α_L (CD11a), α_4 (CD49d)
361 and β_1 (CD29) integrins as compared to endogenous CD8⁺ T cells (**Fig. 6B**). While mandLN-
362 primed OT-I showed highest CD11a levels, MLN- and to a lesser extent spleen-primed T_{EFF}
363 expressed high levels of α_4 and β_7 integrins (**Fig. 6B**). In contrast, the skin homing receptor

364 cutaneous lymphocyte antigen (CLA) was only induced in popLN T_{EFF}, whereas α 1 integrin
365 expression was only modestly induced by any route of infection (**Fig. S4A**).
366 Next, we examined expression of the activation-induced chemokine receptors CXCR3,
367 CX3CR1 and CXCR6. Irrespective of the route of infection, OT-I T_{EFF} increased CXCR3
368 surface levels (**Fig. 6C**). Furthermore, OT-I T_{EFF} increased CX3CR1 and CXCR6 levels (**Fig.**
369 **6C**), in particular spleen-primed T_{EFF}, which may reflect the high Lm burden in this organ after
370 i.v. infection (**Fig. 1F**). In contrast, we did not find evidence for elevated surface expression
371 of CCR4 and CCR6 in any subset, whereas we detected a minor population of CCR10⁺ MLN
372 T_{EFF} (**Fig. S4**). We further compared effector protein levels in T_{EFF} activated via distinct
373 infection routes. Spleen-primed OT-I T_{EFF} showed the highest proportion of Granzyme B⁺
374 cells (**Fig. 6D**), while mandLN- and popLN-primed T_{EFF} expressed increased levels of TNF α ,
375 IFN- γ , and in case of mandLN T_{EFF} also IL-2 (**Fig. 6D**).

376 To explore in more detail on the gut homing capacity of mandLN T_{EFF}, we examined
377 expression the MAdCAM-1 receptor α ₄ β ₇ using direct labeling of the heterodimer. In line with
378 published observations (8, 25), we confirmed increased α ₄ β ₇ levels on MLN- but not
379 mandLN-primed OT-I T_{EFF} (**Fig. 6E**). Furthermore, while the gut homing chemokine receptor
380 CCR9 was induced in MLN-primed T_{EFF} (29.8 \pm 6.8% mean \pm SEM from 2 independent
381 experiments with n = 8 mice), mandLN-primed OT-I did not increase CCR9 expression (**Fig.**
382 **6E**). We confirmed the lack of a gut-homing phenotype imprinting on CD8⁺ T cells after
383 ingestion of Lm-contaminated food (Fig. S4B). These data demonstrate that in an acute
384 infection, mandLN-primed T_{EFF} do not increase signature chemokine and adhesion receptors
385 associated with homing to intestine or skin, but expressed high cytokine levels.

386

387 *mandLN T_{EFF} home preferentially to SLO, lung and OM but not small intestine*

388 We tested how local imprinting affected the dissemination pattern of T_{EFF} generated at
389 distinct lymphoid priming organs. We isolated congenically marked mandLN- and spleen-
390 primed T_{EFF} isolated from FTY720-treated donor mice at 4 d after infection by the i.o. and i.v.

391 route with Lm-OVA and co-transferred them into i.o. Lm-infected mice (**Fig. 6F**). We chose
392 the i.o. route of infection for recipients in this model, because we wanted to address the
393 homing capacity of T_{EFF} populations to the OM. As an internal control for homing to the
394 intestine, we also co-transferred MLN-primed T_{EFF} generated by i.g. Lm-OVA infection (**Fig.**
395 **S5A**). At d 4 post transfer (d 8 p.i.), we injected fluorescently labeled CD45 mAb prior to
396 mouse culling to distinguish circulating from parenchymal cells and isolated spleen, mandLN,
397 MLN, PP, liver, lung, submandibular salivary glands (SMG), OM and small intestine (SI) of
398 recipient mice (for gating strategy see **Fig. S5B**). Owing to the low recovery rate of MLN-
399 primed T_{EFF} from donor mice, we could transfer only limited numbers of cells and did not
400 detect cells of this effector population in all organs. Therefore, we analyzed mandLN- versus
401 spleen-primed OT-I T_{EFF} homing separately from MLN- versus spleen-primed T_{EFF} homing.
402 When corrected for the input, we recovered on d 8 p.i. more parenchymal mandLN-primed
403 OT-I as compared to spleen-primed OT-I in most recipient organs examined (**Fig. S5C**).
404 While this could indicate an increased tissue infiltration capacity of mandLN-primed T_{EFF}, it
405 might reflect the earlier initiation of the contraction phase in spleen-primed T_{EFF} because of
406 the high pathogen burden associated with i.v. infections (**Fig. 1F**). In support of this, we
407 consistently observed lower CD62L and CD127 but increased KLRG1 expression on
408 recovered spleen-primed OT-I as compared to mandLN-primed OT-I T_{EFF} (**Fig. S5D, E**). We
409 therefore normalized the homing ratios of recovered parenchymal MLN- or mandLN-primed
410 OT-I *versus* spleen-primed OT-I T_{EFF} in the analyzed organs to the mean value of their ratio
411 in recipient spleens. As control, transferred MLN-primed OT-I T_{EFF} were 4.1 ± 0.9 more
412 frequent in SI as compared to transferred spleen-primed OT-I T_{EFF} after normalization to
413 recipient spleen mean ratios (**Fig. 6G**), in line with their high $\alpha_4\beta_7$ and CCR9 expression
414 levels. In addition, MLN-primed T_{EFF} recovery from OM and liver was strongly increased as
415 compared to spleen-primed T_{EFF} ($\times 6.1 \pm 2.3$ and $\times 8.0 \pm 3.3$, respectively), whereas it
416 remained comparable in mandLN, MLN, PP and lungs ($\times 1.1-1.9$) (**Fig. 6G**).

417 Similarly, transferred mandLN-primed OT-I T_{EFF} were more frequent as compared to spleen-
418 primed OT-I T_{EFF} in mandLN (x 2.8 ± 0.6; mean ± SEM), MLN (x 2.4 ± 0.2), and in particular
419 in lungs (x 3.7 ± 0.4) and OM (x 4.2 ± 1.6) (**Fig. 6H, I**). In contrast, mandLN-primed T_{EFF} were
420 underrepresented as compared to spleen-primed T_{EFF} in PP (x 0.8 ± 0.1), liver (x 0.6 ± 1),
421 SMG (x 0.6 ± 0.1) and most prominently in SI (x 0.4 ± 0.1), reflecting low induction of $\alpha_4\beta_7$
422 and CCR9 expression in these cells (**Fig. 6H, I**). Taken together, mandLN- and MLN-primed
423 T_{EFF} generated during infection of the upper and lower GI tract differ markedly in their
424 dissemination pattern, with mandLN T_{EFF} being substantially impaired in SI homing.

425

426 *MandLN stromal cells and DC display low expression of RA-producing enzymes*

427 We further examined the mechanism underlying the low tropism of mandLN-primed T_{EFF} for
428 the lower GI tract. The lymphoid microenvironment including stromal cells and DC provides
429 critical cues for tissue-selective imprinting of effector homing potential. A hallmark of
430 intestinal mucosa-surveilling inductive lymphoid tissue is the RA-mediated induction of gut-
431 homing receptors on activated T cells, which promote their subsequent accumulation in
432 lamina propria, GALT and gLN (8). To characterize the gene expression profile of stromal
433 cells, we performed a single cell RNA sequencing (scRNAseq) analysis of the TER-119⁻
434 CD45⁻ stromal compartment of non-infected mandLN and compared it with stromal cells
435 isolated from resting MLN and as control, skin-draining inguinal, axillary and brachial PLN.
436 Unsupervised clustering of combined stromal scRNAseq data identified multiple Col1a1⁺ and
437 Col1a2⁺ fibroblast-like and Cdh5⁺ vascular cell populations (**Fig. 7A and Fig. S6**). While
438 scRNAseq data suggested comparable expression of the RA-producing enzyme Aldh1a1 in
439 fibroblast-like cells LN of all three sites, expression of Aldh1a2 and Aldh1a3 was higher in
440 MLN than in PLN or mandLN fibroblasts (**Fig. 7B, C**). Furthermore, the transcription factor
441 WT1, which drives expression of Aldh1a1 and Aldh1a2 (49), was mainly expressed in MLN
442 fibroblast-like cells (**Fig. 7B, C**). To corroborate these data, we performed qPCR analysis for
443 RA-generating enzymes on sorted TER-119⁻ CD45⁻ stromal cells isolated from MLN, PLN

444 and mandLN. This analysis confirmed that mRNA levels of all three Aldh1a family members
445 were higher in MLN as compared to PLN and mandLN stromal cells (**Fig. 7D**). Since DC
446 contribute to gut-homing phenotype imprinting in activated T cells (10), we isolated CD45⁺
447 CD11c⁺ MHC-II^{high} DC from MLN, PLN and mandLN and compared mRNA levels of Aldh1a1-
448 3 by qPCR. While Aldh1a1 and Aldh1a3 were expressed at low levels in all CD11c⁺
449 populations, Aldh1a2 mRNA levels were highest in MLN CD11c⁺ cells (**Fig. 7D**). Taken
450 together, the mandLN microenvironment shares with skin-draining PLN the lack of gut-
451 homing imprinting capacity. At the same time, scRNAseq data analysis uncovered increased
452 expression of genes involved in “lymphocyte and monocyte chemotaxis” and “cellular
453 responses to IL-1, IFN- γ and TNF” in *bona fide* mandLN CCL21a⁺ T cell zone reticular cells
454 (TRC; cluster 7 in **Fig. 7A**) as compared to PLN TRC, whereas genes related to “collagen
455 fibril organization” and “negative regulation of DC differentiation” were decreased (**Fig. S7**).
456 In combination with increased expression of genes for “T cell costimulation” in mandLN TRC
457 *versus* MLN TRC (**Fig. S7**), these data support the presence of a pro-inflammatory mandLN
458 microenvironment that facilitates rapid generation of CD8⁺ T_{EFF} against oral pathogens.

459

460 *MandLN T_{EFF} reduce Lm burden in spleen but not MLN and PP*

461 We set out to correlate these data with the protective capacity of mandLN-generated T_{EFF} as
462 compared to those generated in spleen and MLN. We adoptively transferred OT-I CD8⁺ T
463 cells and infected recipient mice separately by i.o., i.v. or i.g. Lm-OVA administration in the
464 presence of FTY720. On day 5 p.i., we isolated OT-I T_{EFF} from mandLN, spleen and MLN,
465 respectively, and transferred equal numbers of effector cells separately into secondary
466 recipient mice, which were subsequently infected with Lm-OVA (**Fig. 8A**). We chose the i.g.
467 route of infection for secondary recipients to induce Lm spread to MLN and PP, as i.v. or i.o.
468 administration of Lm does not result in efficient MLN or intestinal infection (50). This
469 approach thus allowed to address the degree of protection afforded by transferred T_{EFF}
470 against regional (intestinal) *versus* systemic Lm burden, with the caveat of the distinct
471 cytokine and GzmB expression profiles induced by distinct routes of priming (**Fig. 6D**).

472 Irrespective of the priming site, transferred OT-I T_{EFF} showed a comparable reduction of
473 bacterial burden in spleen on d 3 p.i. (**Fig. 8B**), while liver was not strongly infected in our
474 setting (not shown). In contrast, mandLN-primed OT-I T_{EFF} did not confer protection in MLN
475 or PP, similar to results obtained after transfer of splenic-primed OT-I T_{EFF} (**Fig. 8B**). In turn,
476 MLN-primed OT-I T_{EFF} caused a reduction in the percentage of MLN and PP containing
477 detectable Lm in secondary recipients (**Fig. 8B**), suggesting a close correlation of gut-
478 homing receptor expression and protection against intestinal Lm infections. This decrease
479 became significant for bacterial loads in MLN when compared to “no OT-I” or transfer of
480 “mandLN-” and “spleen-primed OT-I T_{EFF}” in side-by-side comparisons ($p < 0.05$, Mann-
481 Whitney). In sum, in our model OT-I T_{EFF} generated in OM-draining mandLN constitute a
482 large fraction of the early circulating T_{EFF} pool after pathogen ingestion. Our findings further
483 indicate that orally primed T_{EFF} are capable to reduce Lm burden in spleen and conceivably
484 other SLO, lung and OM, but do not contribute to substantial protection of the lower GI tract
485 and associated intestinal lymphoid tissue (**Fig. 8C**).
486

487 **Discussion**

488 Antimicrobial immune responses have been extensively examined in the gut, leading to the
489 discovery of site-specific imprinting of the host immune response along the length of the
490 intestinal GI tract. In contrast, there is a lack of information on the initiation of adaptive
491 immune responses after microbial challenge of the OM, the primary site of pathogen
492 encounter of the upper GI tract. Furthermore, it has remained unknown how orally triggered
493 T cell activation affects immunity at distal sites. Here, we performed a comprehensive
494 analysis of the kinetics, magnitude and phenotype of CD8⁺ T cell responses after acute oral
495 exposure to an intracellular pathogen. We also examined the contribution of orally primed
496 CD8⁺ T cells to the early circulating T_{EFF} pool, their dissemination patterns and protective
497 capacity. Our data reveal that after ingestion of *Listeria monocytogenes*, mandLN serve as
498 OM-sentinel lymphoid organs. Our data further show that the mandLN microenvironment
499 supports rapid generation of cytotoxic T_{EFF} with a markedly distinct homing profile from the
500 one imprinted by intestinal lymphoid tissue, further expanding the concept of regional
501 specialization of adaptive immunity along the GI tract.

502 The mucosa lining the oral cavity is the first site of contact with ingested microbes before
503 their passage to the esophagus, stomach and intestinal tract. The presence of lymphatic
504 vessels in the OM suggests a continuous surveillance of regional lymph by sentinel LN (26,
505 51). The sequestration of orally administered Lm in mandLN observed here confirms that
506 lymphatic drainage leads to continuous sampling of oral microbes at this anatomical
507 localization, similar to observations made after oral delivery of *Trypanosoma cruzi* (52, 53). It
508 remains unclear how Lm entry into oral lymphatic vessels is regulated. In the oral cavity, the
509 gingival sulcus, which is the space between the gingiva and teeth, is a particularly vulnerable
510 site exposed to trauma caused by mastication and biting. Its epithelium is non-keratinized
511 and transitions to the junctional epithelium that binds directly to teeth (14, 15). Conceivably,
512 lymphatic vessels below the crevicular epithelium lining the gingival sinus may participate in
513 collecting microbe-containing tissue fluids for transport to mandLN. In addition, the vascular-
514 rich sublingual mucosa has absorptive properties, which is clinically relevant to systemically

515 administer drugs or vaccines (15). Oral microbiota might be collected here for lymphatic
516 transport to regional LN, a process which may be facilitated by the lack of a thick mucus
517 layer as is present in intestinal mucosa. In this context, mice lack tonsils, and lumen-
518 sampling M cells are restricted to nasopharynx-associated lymphoid tissue (NALT) of the
519 nasal cavity (54). Our data further suggest a role for migratory DC in transporting processed
520 microbial Ag from the OM to mandLN. It has been reported that infection with foodborne Lm
521 leads to the appearance of endogenous T_{EFF} in MLN and PP one week post Lm infection
522 (25). We expand these observations here by showing that mandLN harbor activated CD8⁺ T
523 cells within the first 3 d following exposure to a foodborne intracellular pathogen, highlighting
524 the role of mandLN as first line immunological firewall of the upper GI tract.

525 One of the hallmarks of cellular immune responses is the imprinting of tissue-specific homing
526 molecules during T cell activation. In skin-draining LN, sunlight-generated vitamin D3 triggers
527 expression of CCR4, CCR10 and P- and E-selectin ligands, while GALT and gLN process
528 dietary carotenes and retinol to imprint a gut-homing $\alpha_4\beta_7^+$ CCR9⁺ phenotype (9, 55). This
529 remarkable “division of labor” ensures an optimal use of resources by directing T cell
530 responses to the anatomical site of pathogen entry. Most of this paradigm has been
531 established by analyzing lymphocyte activation in lymphoid tissue of the lower GI tract. This
532 raises the question why mandLN differ from those sites, even though both drain lymph from
533 microbe-rich mucosal tissue. One explanation is that the induction of RA-generating
534 enzymes in migratory CD103⁺ DC for gut-homing phenotype imprinting in T cells requires RA
535 generated by epithelial cells of the small intestine (11, 56, 57). Similarly, we observed low
536 expression of RA-producing enzymes in stromal cells of mandLN, suggesting that RA is not
537 present in sufficiently high concentration in oral cavity-draining mandLN to direct substantial
538 T_{EFF} trafficking towards gut. In line with this, mandLN do not only drain lymph from the OM
539 but also of the anterior eye chamber, NALT and cerebrospinal fluid of the central nervous
540 system (CNS) (22, 54, 58, 59) (**Fig. 8C**). This may exert an influence on the expression of
541 genes that direct homing patterns in dendritic and stromal cells, e.g. to minimize loss of CD8⁺
542 T_{EFF} to intestinal sites during CNS inflammation. In support of our findings, i.n. Lm infection

543 leading to Ag presentation in NALT does not confer intestinal immunity (25). In a reverse
544 conclusion, our data, in combination with previous studies (13), suggest that induction of gut-
545 homing molecules is most efficient in lymphoid tissue of the small intestine. This locally
546 defined imprinting restricts massive infiltration of gut mucosal tissue with orally primed CD8⁺
547 T cells reacting to microbial Ag of the upper GI tract, whose microbiomes do not strongly
548 overlap (60). Thus, our data suggest the presence of a “staggered” immune response where
549 acute oral microbial exposure will not induce pre-emptive immune responses in the lower GI
550 tract. Instead, intestinal immune responses are only triggered when microbes pass the
551 stomach barrier and reach the gut.

552 While mandLN stromal cells and DC resemble more their skin-draining LN than gut-draining
553 MLN counterparts, we also uncovered a distinct baseline gene expression signature of skin-
554 draining versus mandLN stroma (Fig. S7), which potentially reflects a higher proinflammatory
555 microenvironment in the latter owing to continuous oral microbiome exposure. In this context,
556 mandLN priming does not induce expression of hallmark receptors involved in skin homing,
557 such as CLA or CCR4, presumably reflecting limited drainage of dermal tissue. Instead,
558 CD8⁺ T_{EFF} primed in mandLN showed efficient homing to other SLO including mandLN and
559 spleen, as well as OM and lung. Although we have focused here on their contribution to early
560 target cell killing in spleen, it is highly probable that these cells contribute to elimination of
561 spreading intracellular infections in all target organs including the respiratory tract. This may
562 be of particular importance for host protection given the close anatomical proximity of the
563 upper airways and the oral cavity, which is exploited by airborne viruses to spread to lungs.
564 As a result, early interception of orally encountered microbes will conceivably contribute to
565 the generation of an early T cell response, which in recent clinical studies has been shown to
566 correlate with efficient immunity and rapid clearance in airborne virus infections (61, 62).
567 An open question is to which extent mandLN priming contributes to the generation of
568 systemic and OM CD8⁺ memory cells. After adoptive transfer of mandLN OT-I T_{EFF} into
569 infection-matched recipients, we recovered memory T cells in spleen but not in MLN or PP
570 (not shown). Furthermore, the requirements for entry into the oral cavity are not well defined

571 to date. Our finding that mandLN-primed T_{EFF} home efficiently to OM despite poor gut homing
572 receptor expression suggests that $\alpha_4\beta_7$ and CCR9 are dispensable for this process. Of note,
573 2PM imaging and confocal imaging identified memory T cells in the OM at > 30 d post i.o. Lm
574 infection (**Video S4; Fig. S8**), suggesting that mandLN may contribute to local memory
575 generation of their surveilled barrier tissue.

576 PP and gLN constitute a complementary surveillance system of the lower GI tract, with PP
577 containing gut lumen-sampling M-cells and gLN draining lymphatic vessels originating in
578 lamina propria. Our data suggest that together with M-cell-containing MALT including tonsils
579 (in humans) and NALT, mandLN form a comparable “dual surveillance” system for the
580 oropharyngeal section of the upper GI tract (**Fig. 8C**). The role for mandLN in this process
581 has thus far remained largely overlooked, since most immunologists use i.v. infection of Lm
582 as a robust systemic infection model or bypass the oral cavity by i.g. infection. Taken
583 together, our study adds to the increasingly acknowledged site-specific imprinting of host
584 immune responses along the length of the GI tract, consistent with an instructional role for
585 the Ag sampling location (6, 13).

586 **Material and methods**

587 *Mice*

588 Male and female C57BL/6JRj (Janvier, Le Genest-Saint-Isle, France), CCR7^{tm1Rfor} (CCR7^{-/-})
589 (63), Tg(Ilgax-Venus)1Mnz “CD11c-YFP” (38) and Tg(Prox1-EGFP)KY221Gsat “Prox1-GFP”
590 (27) mice were used for imaging, as recipients for T cell adoptive transfer or for Lm infection.
591 Polyclonal T cells were isolated from C57BL/6 or C57BL/6-Tg(CAG-EGFP)1Osb/J “GFP”
592 donors (64). Tg(TcraTcrb)1100Mjb “OT-I” TCR mice (37) backcrossed on a GFP⁺, dsRed⁺
593 (65) or tdTom⁺ (66, 67) background were described before (68). Mice expressing the
594 photoconvertible protein Kikume-Green-Red (KikGR) (47) were backcrossed to the OT-I
595 strain. In some experiments, CD45.1, CD90.1 and CD45.1/.2 x CD90.1/.2-expressing OT-I
596 were used. Mice were kept at the central animal facilities of the University of Fribourg. All
597 experimental procedures are approved by the Cantonal Committees for Animal
598 Experimentation and conducted according to federal guidelines (2018_22_FR, 2018_24_FR,
599 2018_27_FR).

600

601 *T cell purification and adoptive transfer*

602 Spleens and LN were dissociated using 70 µm cells strainers, and CD8⁺ T cells were
603 negatively isolated using the EasySepTM Mouse CD8⁺ T cell (Stem Cell Technologies) or
604 MojoSortTM Isolation Kits (BioLegend) according to the manufacturer's protocol. Purity of
605 isolated CD8⁺ T cells was > 90%. For 2PM imaging, polyclonal CD8⁺ T cells were labelled
606 with 20 µM CellTrackerTM Blue (CMAC; 7-amino-4-chloromethylcoumarin; Invitrogen) for 20-
607 30 min at 37° C. For proliferation assays, OT-I T cells were labelled with 5 µM CellTraceTM
608 Violet (Invitrogen) at 37° C for 20-30 min.

609

610 *Bacterial infection and CFU quantification*

611 Lm strain 10403s expressing ovalbumin (Lm-OVA) (28) or GFP (Lm-GFP) (69) and Lm strain
612 EGD-e, carrying a recombinant InIA with S192N and Y369S mutations (Lm-InIAtm) (32) were
613 kindly provided by Dr. Doron Merkler (University of Geneva, Switzerland), Neal M. Alto

614 (University of Texas, Southwestern Medical Center, US) and Colin Hill (University College
615 Cork, Ireland), respectively. Bacteria from glycerol stocks were grown in Brain heart infusion
616 (BHI) medium until mid-log phase was reached. Recipient mice were deprived of food and
617 water for 4 h and 15-30 min before and after infection, respectively. Infections performed by
618 pipetting Lm into the mouth over 1-5 min as described (70) (i.o.; $1 \times 10^6 - 2 \times 10^9$ CFU), by
619 intragastric gavage (i.g.; 2×10^9 CFU), or by i.v. (5×10^3 CFU) or s.c. (1×10^4 CFU) injection.
620 Bacterial suspensions were serially diluted and plated on BHI agar plates to verify the actual
621 number of CFU in the inoculum. For foodborne infection, mice were food- and water-deprived
622 for 4 h prior to infection. Bacteria suspension containing Lm-OVA (2×10^9 CFU) was pipetted
623 over small pieces of the mouse chow ($0.25-0.5 \text{ cm}^3$) and mice were kept individually in cages
624 with minimal bedding for 1-2 h until complete food consumption (71).

625 For CFU quantification, mandLN, MLN, PP and spleen were aseptically harvested,
626 homogenized in 70 μm cell strainers and lysed in sterile water. Alternatively, organs were
627 homogenized using MagNALyser tubes Green Beads (Roche) containing sterile PBS (5000
628 rpm for 1 min). Serial dilutions of homogenates were plated on BHI agar, and colonies were
629 counted after 24 h of incubation at 37°C. For PP, BHI agar plates contained 200 $\mu\text{g}/\text{mL}$
630 streptomycin to prevent gut bacteria contamination, since the 10403s strain is streptomycin
631 resistant. CFU was adjusted according to the dilutions and calculated per number of LN or
632 PP collected. For protection experiments, spleen, liver, PP and MLN were lysed in 2 mL
633 tubes containing one steel bead and 1 mL PBS + 0.1% Tween20 (Sigma-Aldrich, St. Louis,
634 USA), using a QiaTissueLyzer (Qiagen) at 25 Hz, 3 min. Serial dilutions were plated on BHI
635 agar, and colonies were counted after 48 h of incubation at 30°C. For PP, BHI agar plates
636 contained 200 $\mu\text{g}/\text{mL}$ streptomycin. CFU was adjusted according to the dilutions and
637 calculated per g of organ.

638

639 *FTY720 treatment*

640 Lymphocyte egress from lymphoid tissue was blocked by treating mice intraperitoneally with
 641 2 mg/kg FTY720 (Sigma), a sphingosine-1-phosphate receptor 1 (S1PR1) inhibitor, starting
 642 at d 1 p.i. with repeated doses after 48 h.

643

644 *Flow cytometry*

645 LN, PP and spleen were harvested at the indicated time points and single cell suspensions
 646 were obtained by passing organs through 70 µm cell strainers. Red blood cell lysis was
 647 performed on splenocytes. Fc receptors were blocked with purified anti-CD16/CD32 mAb
 648 (2.4G2) in FACS buffer (PBS with 2% FCS, 2 mM EDTA and 0.05% NaN₃) for 10 min. Cell
 649 surface staining was performed on ice for 30 min in the dark, followed by wash in FACS
 650 buffer. Zombie Aqua™, Zombie Violet™ or Zombie Red™ (BioLegend) were used to
 651 discriminate live and dead cells. After staining, cells were fixed for 20 min with 4% PFA,
 652 washed and resuspended in PBS. Acquisition was performed using LSR Fortessa (BD
 653 Bioscience), LSR II (BD Bioscience) or Attune NxT Flow cytometer (Thermo Fisher) and
 654 analyzed using FlowJo (TreeStar) software.

655 For cytokine staining, cells were restimulated *in vitro* with 1 µM SIINFEKL (EMC
 656 Microcollections) in the presence of 5 µg/mL brefeldin A (BioLegend) for 5 h at 37° C, 5%
 657 CO₂. Surface staining was performed in the presence of 5 µg/mL brefeldin A, followed by
 658 fixation with 4% PFA for 20 min on ice. For intracellular staining, cells were permeabilized
 659 with 1x PermWash solution (BD Biosciences). Staining for CCR8, CX3CR1, CXCR6, CCR4,
 660 CCR7, CCR10 and CCR6 was performed for 1 h at 37°C.

Antibody/streptavidin	Fluorochrome	Clone	Concentration (µg/mL)	Company	Reference number
CCR10	PE	248918	1:20 dilution	R&D	FAB2815P
CCR8 (CD198)	BV421	SA214G2	2	BioLegend	150305
CD103	APC	2 E7	2	BioLegend	121414
CD103	BV421	2E7.	2	Biolegend	121422
CD11a (integrin αL)	BV605	M17/4	1	BD Biosciences	740347
CD11b	PE-Cy7	M1/70	0.4	BioLegend	101215/101216

CD11c	BV605	N418	2	BioLegend	117334
CD127	APC	A7R34	2	BioLegend	135012
CD186 (CXCR6)	BV711	SA051D1	2	BioLegend	151111
CD19	biotinylated	6D5	5	BioLegend	115503
CD194 (CCR4)	biotinylated	2G12	10	BioLegend	131216
CD196 (CCR6)	PE-Cy7	29-2L17	2	BioLegend	129816
CD197 (CCR7)	PerCP/Cy5.5	4B12	5	BioLegend	120105
CD199 (CCR9)	PE-Cy7	CW1.2	1	BioLegend	128711
CD25	APC	PC61	1-2	BioLegend	102012
CD29 (integrin β 1)	AF488	HM β 1-1	2.5	BioLegend	102211
CD3	PerCP/Cy5.5	17A2	2	BioLegend	100217
CD44	biotinylated	IM7	2.5	BD Biosciences	553132
CD44	PerCP	IM7	2	BioLegend	103036
CD44	PerCP-Cy5.5		2	BioLegend	103032
CD44	BV605	IM7	1-2	BioLegend	103047
CD45	PE-Cy5	30-F11	2.5 μ g/mouse i.v.	BioLegend	103110
CD45.1	PE	A20	1	BioLegend	110708
CD45.1	BV785	A20	1	BioLegend	110743
CD45.1	FITC	A20	2.5	BioLegend	110706
CD45.2	AF488	A20	2.5	BioLegend	110718
CD45.2	BUV395	104	1	BD Biosciences	564616
CD45R (B220)	AF647	RA3-6B2	1	BioLegend	103229
CD49a (integrin α 1)	BUV496	Ha31/8	4	BD Biosciences	741111
CD49d (integrin α 4)	PE/Cy7	R1-2	2	BioLegend	103617
CD62L	BV421	MEL-14	0.5	BioLegend	104436
CD62L	AF488	MEL-14	2.5	BioLegend	104420
CD69	BV711	H1.2F3	1	BioLegend	104537
CD69	PE	H1.2F3	1	BioLegend	104508
CD69	APC-Cy7	H1.2F3	2	BioLegend	104526
CD80	FITC	16-10A1	2.5	BioLegend	104705
CD86	APC-Fire 750	GL-1	1	BioLegend	105045
CD8 α	APC/Fire 750	53-6.7	1	BioLegend	100766
CD8 α	BV711	53-6.7	0.5	BioLegend	100748
CD90.1	BV711	OX-7	0.1	BioLegend	202539
CD90.2	Pacific blue	53-2.1	0.25	BioLegend	140306

CLA (cutaneous lymphocyte antigen)	AF647	HECA-452	1	BioLegend	321310
CX3CR1	BV650	SA011F11	2	BioLegend	149033
CXCR3 (CD183)	BV510	CXCR3-173	2	BioLegend	126527
CXCR3 (CD183)	BV605	CXCR3-173	2-4	BioLegend	126523
Granzyme B	AF647	GB11	2	BioLegend	515405
Granzyme B	FITC	GB11	2	BioLegend	515403
I-A/I-E (MHCII)	BV421	M5/114.15.2	0.5	BioLegend	107632
I-A/I-E (MHCII)	APC-Cy7	M5/114.15.2	0.2	BioLegend	107628
IFN- γ	BV711	XMG1.2	1	BioLegend	505835/6
IL-2	PE	JES6-5H4	2	BioLegend	503807
KLRG1	PE-Cy7	2F1	1	BioLegend	138415
LPAM-1 (Itga4b7)	APC	DATK32	2	eBioscience	17-5887-82
Ly6C	AF700	HK1.4	0.6	BioLegend	128024
Ly6G	biotinylated	1A8	2.5	BioLegend	127603
Ly-6G/C	biotinylated	Gr-1	2.5	BioLegend	108403
NK1.1	PE	PK136	1	BioLegend	108707
NK1.1	biotinylated	PK136	2.5	BioLegend	108703
Rabbit IgG	AF568	polyclonal	5	Thermo Fisher	A11011
RFP	purified	polyclonal	2	Abcam	ab62341
SIRPalpha/CD172a	AF488	P84	2	BioLegend	144023
Streptavidin	BV711	_	0.5	BioLegend	405241
Streptavidin	PE	_	2	BioLegend	405203
Streptavidin	BUV737	_	1	BD Biosciences	564293
Streptavidin	AF488	_	2	Thermo Fisher	S11223
TCR β	biotinylated	H57-597	2.5	BioLegend	109203
TNF- α	BV421	MP6-XT22	1	BioLegend	506328
XCR1	BV785	ZET	2	BioLegend	148225
β 7	biotinylated	FIB504	1.25	BioLegend	321209

661 **Table 1.**

662 For flow cytometry analysis of DC, LN were cut in small fragments and digested in type IV
663 collagenase (1 mg/mL, Worthington) and DNase I (100 U/mL; Roche) in 24-well plates under
664 rotation at 20 rpm for 15-20 min at 37°C. Tissue fragments were dissociated by pipetting
665 using a Pasteur pipette and incubated for additional 15 min. In case tissue fragments were
666 not completely dissociated by pipetting, samples were incubated for additional 10 min. For

667 sorting of DC and stromal cells, we used collagenase P (0.5 mg/mL; Roche), Dispase II (0.5
668 mg/mL; Roche) and DNase I (100 U/mL; Roche) for digestion in a 5 mL round bottom tube.
669

670 *Intravital imaging of mandLN and gingiva*

671 Mice were anesthetized by i.p. injection of 8-10 μ L/g ketamine (20 mg/mL) and xylazine (1
672 mg/mL) and after 15 min, 30 μ L i.p. of acepromazine (2.5 mg/mL). Anesthesia was
673 supplemented when needed with ketamine/xylazine (half dose of xylazine). The fur was
674 removed from the operating area using an electric razor followed by hair removal cream.
675 Mice were placed on a customized stage used for submandibular salivary gland (SMG)
676 imaging (36). Neck and teeth were fixed to reduce shifting. To expose mandLN, a 0.5-1 cm
677 incision was made along the neck region in the skin above the left lobe of the SMG. Under
678 the stereomicroscope, the connective tissue between left and right lobes of the SMG, and
679 between the left lobe and the adjacent skin was disrupted to set the left lobe free. The
680 mandLN and surrounding blood and lymph vasculature were kept untouched and moist with
681 saline during the surgical procedure. The left lobe of the SMG was pulled on top of a
682 coverslip on a holder and glued using veterinary adhesive (Vetbond, M3). A ring of grease
683 (Glisseal N, VWR) was made to create space to be filled with saline and keep tissue moist.
684 The SMG was fixed in a position to expose the mandLN and for removal of fat tissue. A
685 coverslip was placed on top, slightly touching the LN without impairing blood supply. To
686 maintain tissue at 35-38°C, a heating ring was placed on top as described for other LN
687 surgeries (72).

688 To expose the gingiva, a 0.5 cm incision was made in the lower lip using an electric
689 cauterizer. Sutures were tied to both sides and fixed into the surface of the surgical stage to
690 stretch the area and expose the inferior teeth. Viscotears (Alcon) was used to keep tissue
691 moist and a holder with a coverslip and heating ring was placed on top. For two-photon
692 microscopy (2PM) imaging of Lm accumulation in mandLN, we surgically prepared mice to
693 expose gingiva and mandLN as described above and added $4-8 \times 10^6$ CFU Lm-GFP in 10 μ L
694 onto the gingiva. 2PM was performed with an Olympus BX50WI microscope equipped with

695 20X Olympus (NA 0.95) or 25X Nikon (NA 1.10) objectives and a TrimScope 2PM system
696 controlled by ImSpector software (LaVisionBiotec). Prior to recording, Alexa Fluor 633- or
697 Alexa Fluor 488 conjugated MECA-79 (10 µg/mouse) was injected i.v. to label high
698 endothelial venules (HEV). For excitation, a Ti:sapphire laser (Mai Tai HP) was tuned to 780
699 or 840 nm. For 4-dimensional analysis of cell migration, 11 to 16 x-y sections with z-spacing
700 of 4 µm were acquired every 20 s for 20-30 min with a field of view of 150-350 x 150-350 µm.
701 Emitted light and second harmonic generation (SHG) signals were detected through 447/55
702 nm, 525/50 nm, 593/40 nm and 655/40 nm bandpass filters with non-scanned detectors
703 when using C57BL/6 recipient mice. For CD11c-YFP⁺ recipient mice, 447/55 nm, 513/20 nm,
704 543/39 nm and 624/30 nm were used as bandpass filters. Second harmonic generation or
705 HEV signals were used as anatomical reference channel for real-time offset correction to
706 minimize tissue shift (73). Sequences of image stacks were transformed into volume-
707 rendered four-dimensional videos with using Imaris software (Bitplane), which was also used
708 for semi-automated tracking of cell motility in three dimensions. Cell centroid data was used
709 to calculate key parameters of cell motility using Matlab (R2019b, MathWorks). Speed was
710 defined as total track length divided by total track duration in µm/min. The arrest coefficient
711 was derived from the percentage of time a cell is migrating below a motility threshold speed
712 of 5 µm/min. Meandering index was calculated by dividing displacement by track length.
713 Since the meandering index is influenced by track duration, we calculated the corrected track
714 straightness defined as meandering index multiplied by the square root of cell track duration
715 (41).

716

717 *Stereomicroscope imaging*

718 MandLN and gingiva were exposed and pictures were taken using a Leica MZ16 FA
719 stereomicroscope equipped with color high resolution camera (Leica). Images were
720 processed using Adobe Photoshop CS6.

721

722 *Immunofluorescence*

723 Mice were anesthetized with i.p. injection of ketamine and xylazine and perfused with cold
724 2% PFA. MandLN were harvested and fixed overnight in 4% PFA, and dehydrated in 30%
725 sucrose o.n. prior to embedding in TissueTek O.C.T. compound (Sakura) for cryostat
726 sectioning. Slides with 10 μ m-thick cryosections were mounted with ProLong™ Gold Antifade
727 Mountant (Molecular Probes). Fluorescence microscopy was performed using Leica SP5
728 confocal microscope with 20X (NA 0.7) and 63X (NA 1.3) Leica objectives. Images were
729 processed using Adobe Photoshop CS6 and Imaris 8.4.1 (Bitplane). Brightness and contrast
730 were adjusted for each image individually.

731 Gingival tissues anterior to the incisors teeth, buccal mucosa, palate and tongue were
732 harvested. Tissues were fixed in 4% PFA for 4-6 h under agitation at 4° C and embedded in
733 TissueTek O.C.T. compound (Sakura) for cryostat sectioning. Slides with 6 μ m-thick
734 cryosections were fixed with 4% PFA for 15 min at RT. After three washing steps, PFA was
735 quenched by adding 0.1 M Glycine for 15 min. Sections were permeabilized for 15-30 min
736 with PBS + 0.2% Triton-X 100 and washed three times. Samples were incubated with
737 blocking solution (PBS with 2% BSA and 10% donkey serum) for 45-60 min at RT. Primary
738 purified antibody anti-RFP (Abcam; ab62341) diluted in blocking solution was added and
739 kept overnight at 4° C. After three washing steps, sections were incubated with secondary
740 AF568 donkey anti-rabbit Ab (Invitrogen A11011) diluted in blocking solution for 5 h at RT.
741 After three more washing steps, slides were mounted with ProLong™ Gold Antifade
742 Mountant (Molecular Probes). Fluorescence microscopy was performed using the Stellaris 8
743 confocal microscope with 63X objective (Leica). Images were processed using Adobe
744 Photoshop CS6 and Imaris 8.4.1 (Bitplane).

745

746 *Photoconversion*

747 C57BL/6 mice received i.v. injections of 7×10^6 naïve KikGR OT-I cells before i.o. infection of
748 Lm-OVA (2×10^9 CFU) on the following day. At day 3 p.i., the fur of anaesthetized mice was
749 removed in the neck area using an electric razor followed by hair removal cream. A sagittal
750 incision of approximately 1-2 cm length was made at the height of SMG and tissue around

751 the mandLN was gently removed. MandLN were photoconverted with a spot lamp system
752 (BlueWave 200, Dymax) using a 433/24 filter (AHF) with 260 mW/m² for 3 min. The same
753 procedure was performed on the contralateral side. The incision was closed using veterinary
754 adhesive (Vetbond, M3) and mice were allowed to rest. After 14 h, organs were harvested for
755 flow cytometry.

756

757 *Adoptive transfer of mandLN-, spleen- and MLN-primed OT-I T_{EFF}*

758 CD45.1, CD90.1 or CD45.1/.2 x CD90.1/.2 OT-I T_{EFF} were obtained at d 4 p.i. from mandLN
759 (i.o.), spleen (i.v.) and MLN (i.g.) of FTY720-treated C57BL/6 mice by magnetic bead sorting
760 of CD8⁺ T cells in medium containing 25 µg/mL of anti-ARTC2 Nanobody (Biolegend).

761 MandLN-, spleen- and MLN-primed OT-I T_{EFF} (0.7 – 7 x 10⁵ each/mouse) were co-
762 transferred into d 4 i.o.-infected age- and sex-matched recipients. At d 8 (4 d after OT-I T_{EFF}
763 transfer), mice received CD45 i.v. 3-5 min before euthanasia to label leukocytes in blood.

764 OM, lung, liver, SMG, small intestine, PP, mandLN, MLN and spleen were harvested for flow
765 cytometry. Cell frequencies were normalized to the input.

766

767 *Lymphocyte isolation from non-lymphoid tissues*

768 OM (buccal mucosa, maxillary and mandibular molar areas with surrounding gingiva, palate
769 and tongue) was dissected and enzymatically digested with 1 mL of 0.5 mg/mL Liberase DL
770 (Roche) for 20 min followed by addition 1 mL of 0.5 mg/mL Liberase TL (Roche) for another
771 20 min at 37° C under rotation. Digestion was stopped by addition of 1 mM EDTA. Gingival
772 tissues were removed from each block of tissue, using fine surgical forceps. Digested tissues
773 were filtered through a 70-µm cell strainer. Isolated cells were passed through a density
774 gradient with 40 and 70% Percoll (Cytiva) for 20 min at 700 g. The interphase containing
775 lymphocytes was collected, washed, and resuspended in cell culture media containing
776 DNase I before further analysis (16, 74).

777 For small intestine, small intestinal intraepithelial lymphocytes (IEL) and lamina propria
778 lymphocytes (LPL) were isolated as previously described with minor modifications (75). The

779 small intestine was opened longitudinally and feces removed by rinsing the tissue with
780 HBSS/5% FCS. After removing PP, IEL were isolated by incubating the small intestinal tissue
781 for 18 min in 30 mL HBSS/2 mM dithiothreitol/0.5 mM EDTA/5% FBS at 37° C under rotation.
782 IEL were enriched using 40 and 70% Percoll (Cytiva) for 20 min at 700 g. IEL were collected
783 from the interphase and kept in HBSS/5% FCS containing DNase I on ice. Tissue pieces
784 were digested in 30 mL HBSS/5% FBS/1.3 mM CaCl₂/0.5 mM MgCl₂/0.6 mM
785 MgSO₄/Collagenase IV (1mg/mL, Sigma-Aldrich)/ DNase I (20 µg/mL, Roche) for 20 min at
786 37° C under rotation. LPL single-cell suspension was pelleted, resuspended in HBSS/5%
787 FCS/DNase I and stored on ice for further processing. Enriched IEL were pooled with LPL as
788 small intestine lymphocytes.

789 Liver was cut and dissociated using a 70-µm cell strainer (adding 10 mL ice cold RPMI four
790 times). Samples were resuspended in 10 mL RPMI containing 2 mg collagenase IV (Sigma-
791 Aldrich) and 6.25 µg DNase (Roche). Tissue homogenates were vortexed and incubated at
792 37°C for 40 min (vortexing every 10 min). After digestion, 25 mL RPMI was added, samples
793 were vortexed and centrifuged at 20 g for 3 min to allow only the connective tissue to pellet.
794 Supernatant was transferred to a new tube and centrifuged at 540 g for 5 min. The pellet was
795 resuspended in 4 mL 40% Percoll (Cytiva) and centrifuged at 1000 g for 20 min. The
796 leukocyte pellet was lysed with RBC lysis buffer, washed and resuspended in RPMI/5% FCS.

797 Lung tissue was cut in small fragments and digested in 5 mL of RPMI/5% FCS/Collagenase
798 type IV (1 mg/mL; Sigma-Aldrich)/Dispase II (0.5 mg/mL; Roche)/DNase I (1 kU/mL; Roche)
799 for 45 min at 37°C under rotation. Tissue fragments were dissociated by pipetting every 15
800 min, first using a 5 mL serological pipette, followed by a P1000 microtiter pipette at the
801 second and last rounds of pipetting. After complete dissociation of tissue fragments,
802 digestion was stopped by adding 5 mL of 5 mM EDTA. Cells were resuspended in 7 mL 40%
803 Percoll (Cytiva), with 2.5 mL 70% Percoll laid underneath, and spun down for 20 min at 1000
804 g. Cells at the interphase were collected, washed and resuspend in 1 mL of RPMI/5% FCS.

805 SMG was cut in small pieces and transferred to an Eppendorf tube containing 1mL of
806 digestion mix (RPMI/5% FCS/ collagenase II (2 kU/mL; Gibco)/DNase I (1 kU/mL; Roche).

807 Samples were incubated for 30 min at 37°C under rotation with vortexing every 5 min.
808 Remaining tissue was passed through a 70 µm cell strainer and washed with 15 mL of PBS/5
809 mM EDTA. Pellet was resuspended in CMR (RPMI supplemented with 10% FCS/10 mM
810 HEPES/2 mM L-Glu/10 mM Na-pyruvate/50 µM β-ME/NEAA and PenStrep).

811

812 *B cell killing assay*

813 C57BL/6 mice treated with or without 200 µg Mel-14 (BioXCell; injected i.p. 4 h before cell
814 transfer) received i.v. 3×10^6 OT-I cells. The following day, mice were i.o. infected with $2 \times$
815 10^9 CFU of Lm-OVA. B cells were isolated from sex-matched C57BL/6 donor mice using
816 MojoSort™ Mouse Pan B Cell Isolation kit II (BioLegend) and pulsed or not with 100 nM
817 OVA₂₅₇₋₂₆₄ (EMC Microcollections). Pulsed and unpulsed B cells were stained with 1 and 7.5
818 µM CFDA SE Cell Tracker Kit (Molecular Probes), respectively, and 5×10^6 cells of each
819 were injected i.v. (1:1 ratio) into d 3-infected recipients. After 12 h, lymphoid organs were
820 harvested for flow cytometry analysis.

821

822 *Single cell gene expression and data analysis*

823 Single cell gene expression of TER119⁻ CD45⁻ stromal cells was measured using the 10x
824 Chromium system, with the Next GEM Single Cell 3' Reagent Kit v3.1 (10x Genomics,
825 Pleasanton, CA, USA). GEM generation and barcoding, reverse transcription, cDNA
826 amplification and 3' Gene Expression library generation steps were all performed according
827 to the manufacturer's user guide. Specifically, the designated volume of each cell suspension
828 (800 -1200 cells/µL) and nuclease-free water was used for a targeted cell recovery of 10'000
829 cells according to the Cell Suspension Volume Calculator Table of the abovementioned user
830 guide. GEM generation was followed by a GEM-reverse transcription incubation, a clean-up
831 step and 15 cycles of cDNA amplification. The quality and quantity of the cDNA was
832 assessed using fluorometry and capillary electrophoresis, respectively. The barcoded cDNA
833 libraries were pooled and sequenced paired-end and single indexed on an Illumina NovaSeq
834 6000 sequencer using a S2 flowcell (100 cycles). The read setup was as follows: read 1: 28

835 cycles, i7 index: 8 cycles, i5: 0 cycles and read 2: 91 cycles. An average of 740,045,087
836 reads/library were obtained, which corresponds to an average of 74,091 reads/cell.
837 Mapping and counting of the UMIs for the samples from mandLN, MLN and PLN were
838 performed using Cellranger (version 3.0.2, 10x Genomics) with the reference genome
839 GRCm38.93 from Ensembl to build the necessary index files. Subsequent analysis was
840 performed in R (version 4.0.2) (76). The Scater package (version 1.14) (77) was used to
841 assess the proportion of ribosomal and mitochondrial genes as well as the number of
842 detected genes. Cells were considered as outliers and filtered out if the value of the
843 proportion of expressed mitochondrial genes or the number detected genes deviated more
844 than three median absolute deviations from the median across all cells. After quality control,
845 the sample from mandLN retained 4434 cells, the sample from MLN retained 10058 cells and
846 the sample from PLN retained 7750 cells. Normalization between samples was done with the
847 deconvolution method of Lun et al. (78) using the package Scraper (version 1.14) (79).
848 Samples were integrated with the FindIntegrationAnchors function of the package Seurat
849 (version 3.1) based on the first 20 principal components (PCs) (80). Graph-based clustering
850 was done with the FindNeighbors and FindClusters functions of the Seurat package using
851 the first 40 PCs from the dimensionality reduction step. The Clustree package (version 0.4)
852 (81) was used to determine the resolution resulting in clustering concurring with the
853 presumed cell types, which was 0.4. Clusters were manually annotated based on marker
854 genes that were identified with the FindMarkers function of Seurat. Following this, seven
855 clusters were removed from the analysis as they represented hematopoietic cells. The
856 remaining cells were re-clustered in an identical fashion but with a resolution of 0.3. The
857 dataset has been deposited on ENA (project ID: PRJEB40464).

858

859 *Quantitative PCR*

860 For sorting of DC and stromal cells, cell suspensions were stained with mAbs and propidium
861 iodide to discriminate between live *versus* dead cells. CD45⁺ MHC-II^{high} CD11c⁺ DCs and

862 CD45⁻ stromal cells were sorted using a FACSAria Fusion (BD). For qPCR, the total RNA
 863 from 2.7-30 x 10⁴ sorted DC and stromal cells was extracted using Trizol Reagent (Sigma-
 864 Aldrich) and coprecipitant GlycoBlue™ (Invitrogen). Reverse transcriptase reactions were
 865 performed using High-Capacity cDNA Reverse Transcription kit (Applied Biosystems, USA)
 866 according to the manufacturer's instructions. qPCR assays were performed on StepOnePlus
 867 (Applied Biosystems, USA) using FastStart Universal SYBR Green Master (Rox) (Roche,
 868 Switzerland). QuantiNova LNA-enhanced primers for *Aldh1a1*, *Aldh1a2*, *Aldh1a3* and as
 869 endogenous housekeeping reference gene hypoxanthine-guanine phosphoribosyltransferase
 870 (HPRT) were purchased from Qiagen (Germany) (**Table 2**). qPCR reactions were performed
 871 in duplicates in a total volume of 20 µL. The cycling conditions were: 95°C for 10 min,
 872 followed by 40 cycles at 95°C for 10 s and 60°C for 30 s. After amplification, dissociation
 873 curves were performed to monitor primer specificity, revealing only one melting peak for each
 874 amplified fragment. qPCR data were normalized to the housekeeping gene HPRT and the
 875 relative changes in mRNA expression were calculated by 2^{-ΔCt}.

Assay Name	Full name	Gene ID	Ref Seq	Catalogue #
MM_HPRT_2521490	hypoxanthine guanine phosphoribosyl transferase	15452	NM_013556	SBM1225379
MM_ALDH1A1_20456 06	aldehyde dehydrogenase family 1, subfamily A1	11668	NM_001361506	SBM0801506
MM_ALDH1A2_19667 74	aldehyde dehydrogenase family 1, subfamily A2	19378	NM_009022	SBM0722689
MM_ALDH1A3_21256 65	aldehyde dehydrogenase family 1, subfamily A3p	56847	NM_053080	SBM0881559

876 **Table 2.**

877

878 *Statistical analysis*

879 Student's t-test, Mann-Whitney U-test, ANOVA, Kruskal-Wallis and Wilcoxon tests were used
 880 to determine statistical significance as indicated (Prism, GraphPad). Significance threshold
 881 was set at p < 0.05.

882

883 *Data availability statement*

884 All datasets (beyond the data provided in the “RawDataFile” and the ENA repository) are
885 available through JVS.

886

887 *Supplemental material*

888 Fig. S1. Depiction of surgery for gingiva and mandLN.

889 Fig. S2. Flow cytometry of DC and CD8⁺ T cell subsets.

890 Fig. S3. CD8⁺ T cell activation with distinct Lm inocula and food consumption.

891 Fig. S4. Expression of trafficking and effector markers on orally primed OT-I T cells.

892 Fig. S5. Adoptive transfer of T_{EFF} primed with distinct routes of infection.

893 Fig. S6. scRNAseq data on expression of selected genes of interests in SLO stromal cells.

894 Fig. S7. Differentially expressed genes in TRC of mandLN, MLN and PLN.

895 Fig. S8. Confocal images of memory CD8⁺ T cells in OM.

896 Video S1. OT-I in uninfected mandLN.

897 Video S2. OT-I in mandLN on d 2 post i.o. Lm infection.

898 Video S3. OT-I in mandLN on d 3 post i.o. Lm infection.

899 Video S4. OT-I in gingiva in memory phase.

900 **Author contribution**

901 JBdA performed experiments with help from LMA, JA, DvW, SW, and JMM. JA, GvG and DF
902 performed scRNAseq analysis under supervision of RB. XF and MI provided a script for cell
903 tracking analysis. JBdA, CM and JVS designed experiments and wrote the manuscript with
904 input from all coauthors.

905

906 **Acknowledgments**

907 This work benefitted from the BioImage Light Microscopy Facility and Cell Analytics Facility
908 of the University of Fribourg. We thank Danièla Grand, Antoinette Hayoz and Pablo Bànicles
909 for expert technical assistance, Pamela Nicholson, Catia Coito, Marion Ernst and Daniela
910 Steiner from the Next-Generation Sequencing Platform of the University of Bern and Dr.
911 Doron Merkler, Neal Alto and Colin Hill for sharing Listeria strains.

912

913 **Funding**

914 This work was funded by Swiss National Foundation (SNF) project grant 31003A_172994,
915 Sinergia project CRSII5_170969 (to JVS and RB), SNF project grant 314730_189277 (to
916 CM), the Brazilian PhD Exchange Scholarship from Research Support Foundation of Rio de
917 Janeiro State (FAPERJ), a Swiss Government Excellence Scholarship and a Young
918 Investigator Grant from Novartis Foundation for Medical-Biological Research (application
919 #21B101) (to JBdA). MI is supported by European Research Council (ERC) consolidator
920 grant 725038, Italian Association for Cancer Research (AIRC) grants 1989 and 22737, Italian
921 Ministry of Health (MoH) grant RF-2018-12365801, Lombardy Foundation for Biomedical
922 research (FRRB) grant 2015-0010, the European Molecular Biology Organization Young
923 Investigator Program, and a Career Development from the Giovanni Armenise-Harvard
924 Foundation. XF is supported by a postdoctoral fellowship from AIRC and Marie Skłodowska-
925 Curie actions (COFUND grant 23906). M.I. participates in advisory boards/consultancies for
926 Gilead Sciences, Roche, Third Rock Ventures, Amgen, Allovir, Asher Bio, ENYO Pharma.

927 **References**

- 928 1. H. Kiyono, T. Azegami, The mucosal immune system: From dentistry to vaccine
929 development, *Proc. Jpn. Acad., Ser. B, Phys. Biol. Sci.* **91**, 423–439 (2015).
- 930 2. A. M. C. Faria, B. S. Reis, D. Mucida, Tissue adaptation: Implications for gut immunity and
931 tolerance, *Journal of Experimental Medicine* **214**, 1211–1226 (2017).
- 932 3. Y. Belkaid, O. J. Harrison, Homeostatic Immunity and the Microbiota, *Immunity* **46**, 562–
933 576 (2017).
- 934 4. O. Schulz, O. Pabst, Antigen sampling in the small intestine, *Trends Immunol* **34**, 155–161
935 (2013).
- 936 5. M. Shale, C. Schiering, F. Powrie, CD4(+) T-cell subsets in intestinal inflammation,
937 *Immunol Rev* **252**, 164–182 (2013).
- 938 6. A. M. Mowat, W. W. Agace, Regional specialization within the intestinal immune system,
939 *Nat Rev Immunol* **14**, 667–685 (2014).
- 940 7. P. Brandtzaeg, H. Kiyono, R. Pabst, M. W. Russell, Terminology: nomenclature of
941 mucosa-associated lymphoid tissue, *Mucosal Immunol* **1**, 31–37 (2008).
- 942 8. J. R. Mora, M. R. Bono, N. Manjunath, W. Weninger, L. L. Cavanagh, M. Roseblatt, U.
943 H. von Andrian, Selective imprinting of gut-homing T cells by Peyer's patch dendritic cells,
944 *Nature* **424**, 88–93 (2003).
- 945 9. M. Iwata, A. Hirakiyama, Y. Eshima, H. Kagechika, C. Kato, S.-Y. Song, Retinoic acid
946 imprints gut-homing specificity on T cells, *Immunity* **21**, 527–538 (2004).
- 947 10. M. N. Erkelens, R. E. Mebius, Retinoic Acid and Immune Homeostasis: A Balancing Act,
948 *Trends Immunol* **38**, 168–180 (2017).
- 949 11. A. Larange, H. Cheroutre, Retinoic Acid and Retinoic Acid Receptors as Pleiotropic
950 Modulators of the Immune System, *Annu. Rev. Immunol.* **34**, 369–394 (2016).
- 951 12. S. A. Houston, V. Cerovic, C. Thomson, J. Brewer, A. M. Mowat, S. Milling, The lymph
952 nodes draining the small intestine and colon are anatomically separate and immunologically
953 distinct, *Mucosal Immunol* **9**, 468–478 (2016).
- 954 13. D. Esterhazy, M. C. C. Canesso, L. Mesin, P. A. Muller, T. B. R. de Castro, A. Lockhart,
955 M. ElJalby, A. M. C. Faria, D. Mucida, Compartmentalized gut lymph node drainage dictates
956 adaptive immune responses, *Nature* **569**, 126–130 (2019).
- 957 14. N. M. Moutsopoulos, J. E. Konkel, Tissue-Specific Immunity at the Oral Mucosal Barrier,
958 *Trends Immunol* **39**, 276–287 (2018).
- 959 15. S. L. Gaffen, N. M. Moutsopoulos, Regulation of host-microbe interactions at oral
960 mucosal barriers by type 17 immunity, *Sci Immunol* **5**, eaau4594 (2020).
- 961 16. J.-Y. Park, H. Chung, Y. Choi, J.-H. Park, Phenotype and Tissue Residency of
962 Lymphocytes in the Murine Oral Mucosa, *Front. Immun.* **8**, 1628–10 (2017).
- 963 17. S. Kitamoto, H. Nagao-Kitamoto, Y. Jiao, M. G. Gilliland, A. Hayashi, J. Imai, K.
964 Sugihara, M. Miyoshi, J. C. Brazil, P. Kuffa, B. D. Hill, S. M. Rizvi, F. Wen, S. Bishu, N.
965 Inohara, K. A. Eaton, A. Nusrat, Y. L. Lei, W. V. Giannobile, N. Kamada, The Intermucosal

- 966 Connection between the Mouth and Gut in Commensal Pathobiont-Driven Colitis, *Cell* **182**,
967 447–462.e14 (2020).
- 968 18. S. S. Lakdawala, A. Jayaraman, R. A. Halpin, E. W. Lamirande, A. R. Shih, T. B.
969 Stockwell, X. Lin, A. Simenauer, C. T. Hanson, L. Vogel, M. Paskel, M. Minai, I. Moore, M.
970 Orandle, S. R. Das, D. E. Wentworth, R. Sasisekharan, K. Subbarao, The soft palate is an
971 important site of adaptation for transmissible influenza viruses, *Nature* **526**, 122–125 (2015).
- 972 19. N. Huang, P. Pérez, T. Kato, Y. Mikami, K. Okuda, R. C. Gilmore, C. D. Conde, B.
973 Gasmi, S. Stein, M. Beach, E. Pelayo, J. O. Maldonado, B. A. Lafont, S.-I. Jang, N. Nasir, R.
974 J. Padilla, V. A. Murrah, R. Maile, W. Lovell, S. M. Wallet, N. M. Bowman, S. L. Meinig, M. C.
975 Wolfgang, S. N. Choudhury, M. Novotny, B. D. Aevermann, R. H. Scheuermann, G. Cannon,
976 C. W. Anderson, R. E. Lee, J. T. Marchesan, M. Bush, M. Freire, A. J. Kimple, D. L. Herr, J.
977 Rabin, A. Grazioli, S. Das, B. N. French, T. Pranzatelli, J. A. Chiorini, D. E. Kleiner, S.
978 Pittaluga, S. M. Hewitt, P. D. Burbelo, D. Chertow, NIH COVID-19 Autopsy Consortium, HCA
979 Oral and Craniofacial Biological Network, K. Frank, J. Lee, R. C. Boucher, S. A. Teichmann,
980 B. M. Warner, K. M. Byrd, SARS-CoV-2 infection of the oral cavity and saliva, *Nat Med*
981 (2021), doi:10.1038/s41591-021-01296-8.
- 982 20. M. A. Shikanai-Yasuda, N. B. Carvalho, Oral transmission of Chagas disease, *Clin Infect*
983 *Dis* **54**, 845–852 (2012).
- 984 21. L. E. Mkonyi, A. Bletsa, A. I. Bolstad, V. Bakken, H. Wiig, E. Berggreen, Gingival
985 lymphatic drainage protects against Porphyromonas gingivalis-induced bone loss in mice,
986 *American Journal Of Pathology* **181**, 907–916 (2012).
- 987 22. W. Van den Broeck, A. Derore, P. Simoens, Anatomy and nomenclature of murine lymph
988 nodes: Descriptive study and nomenclatory standardization in BALB/cAnNCrl mice, *J*
989 *Immunol Methods* **312**, 12–19 (2006).
- 990 23. M. Lohrberg, J. Wilting, The lymphatic vascular system of the mouse head, *Cell Tissue*
991 *Res* **366**, 667–677 (2016).
- 992 24. S. E. F. D'Orazio, Animal models for oral transmission of Listeria monocytogenes, *Front*
993 *Cell Infect Microbiol* **4**, 15 (2014).
- 994 25. B. S. Sheridan, Q.-M. Pham, Y.-T. Lee, L. S. Cauley, L. Puddington, L. Lefrançois, Oral
995 infection drives a distinct population of intestinal resident memory CD8(+) T cells with
996 enhanced protective function, *Immunity* **40**, 747–757 (2014).
- 997 26. N. Ushijima, K. Inoue, T. Domon, S. Yoshida, Distribution and organization of lymphatic
998 vessels in the mouse gingiva: An immunohistochemical study with LYVE-1, *Archives of Oral*
999 *Biology* **53**, 652–658 (2008).
- 1000 27. I. Choi, H. K. Chung, S. Ramu, H. N. Lee, K. E. Kim, S. Lee, J. Yoo, D. Choi, Y. S. Lee,
1001 B. Aguilar, Y.-K. Hong, Visualization of lymphatic vessels by Prox1-promoter directed GFP
1002 reporter in a bacterial artificial chromosome-based transgenic mouse, *Blood* **117**, 362–365
1003 (2011).
- 1004 28. D. Zehn, S. Y. Lee, M. J. Bevan, Complete but curtailed T-cell response to very low-
1005 affinity antigen, *Nature* **458**, 211–214 (2009).
- 1006 29. H. Saklani-Jusforgues, E. Fontan, P. L. Goossens, Effect of acid-adaptation on Listeria
1007 monocytogenes survival and translocation in a murine intragastric infection model, *FEMS*
1008 *Microbiol. Lett.* **193**, 155–159 (2000).

- 1009 30. M. G. Pitts, S. E. F. D'Orazio, A Comparison of Oral and Intravenous Mouse Models of
1010 Listeriosis, *Pathogens* **7** (2018), doi:10.3390/pathogens7010013.
- 1011 31. T. Wollert, B. Pasche, M. Rochon, S. Deppenmeier, J. van den Heuvel, A. D. Gruber, D.
1012 W. Heinz, A. Lengeling, W.-D. Schubert, Extending the host range of *Listeria monocytogenes*
1013 by rational protein design, *Cell* **129**, 891–902 (2007).
- 1014 32. I. R. Monk, P. G. Casey, C. Hill, C. G. M. Gahan, Directed evolution and targeted
1015 mutagenesis to murinize *Listeria monocytogenes* internalin A for enhanced infectivity in the
1016 murine oral infection model, *BMC Microbiology* **10**, 318–13 (2010).
- 1017 33. C. Bécavin, C. Bouchier, P. Lechat, C. Archambaud, S. Creno, E. Gouin, Z. Wu, A.
1018 Kühbacher, S. Brisse, M. G. Pucciarelli, F. García-del Portillo, T. Hain, D. A. Portnoy, T.
1019 Chakraborty, M. Lecuit, J. Pizarro-Cerdá, I. Moszer, H. Bieme, P. Cossart, Comparison of
1020 widely used *Listeria monocytogenes* strains EGD, 10403S, and EGD-e highlights genomic
1021 variations underlying differences in pathogenicity, *mBio* **5**, e00969–14 (2014).
- 1022 34. R. Förster, A. C. Davalos-Miszlitz, A. Rot, CCR7 and its ligands: balancing immunity and
1023 tolerance, *Nat Rev Immunol* **8**, 362–371 (2008).
- 1024 35. O. Schulz, S. I. Hammerschmidt, G. L. Moschovakis, R. Förster, Chemokines and
1025 Chemokine Receptors in Lymphoid Tissue Dynamics, *Annu. Rev. Immunol.* **34**, 203–242
1026 (2016).
- 1027 36. X. Ficht, F. Thelen, B. Stolp, J. V. Stein, Preparation of Murine Submandibular Salivary
1028 Gland for Upright Intravital Microscopy, *J Vis Exp* (2018), doi:10.3791/57283.
- 1029 37. K. A. Hogquist, S. C. Jameson, W. R. Heath, J. L. Howard, M. J. Bevan, F. R. Carbone, T
1030 cell receptor antagonist peptides induce positive selection, *Cell* **76**, 17–27 (1994).
- 1031 38. R. L. Lindquist, G. Shakhar, D. Dudziak, H. Wardemann, T. Eisenreich, M. L. Dustin, M.
1032 C. Nussenzweig, Visualizing dendritic cell networks in vivo, *Nat Immunol* **5**, 1243–1250
1033 (2004).
- 1034 39. H. D. Moreau, P. Bousso, Visualizing how T cells collect activation signals in vivo, *Curr*
1035 *Opin Immunol* **26**, 56–62 (2014).
- 1036 40. S. Sivapatham, X. Ficht, J. Barreto de Albuquerque, N. Page, D. Merkler, J. V. Stein,
1037 Initial Viral Inoculum Determines Kinapse-and Synapse-Like T Cell Motility in Reactive
1038 Lymph Nodes, *Front. Immun.* **10**, 2086 (2019).
- 1039 41. J. B. Beltman, A. F. M. Marée, R. J. de Boer, Analysing immune cell migration, *Nat Rev*
1040 *Immunol* **9**, 789–798 (2009).
- 1041 42. R. N. Germain, M. J. Miller, M. L. Dustin, M. C. Nussenzweig, Dynamic imaging of the
1042 immune system: progress, pitfalls and promise, *Nature Publishing Group* **6**, 497–507 (2006).
- 1043 43. T. R. Mempel, S. E. Henrickson, U. H. von Andrian, T-cell priming by dendritic cells in
1044 lymph nodes occurs in three distinct phases, *Nature* **427**, 154–159 (2004).
- 1045 44. B. Breart, P. Bousso, Cellular orchestration of T cell priming in lymph nodes, *Curr Opin*
1046 *Immunol* **18**, 483–490 (2006).
- 1047 45. S. E. Henrickson, T. R. Mempel, I. B. Mazo, B. Liu, M. N. Artyomov, H. Zheng, A.
1048 Peixoto, M. P. Flynn, B. Senman, T. Junt, H. C. Wong, A. K. Chakraborty, U. H. von Andrian,

- 1049 T cell sensing of antigen dose governs interactive behavior with dendritic cells and sets a
1050 threshold for T cell activation, *Nat Immunol* **9**, 282–291 (2008).
- 1051 46. B. B. Au-Yeung, J. Zikherman, J. L. Mueller, J. F. Ashouri, M. Matloubian, D. A. Cheng,
1052 Y. Chen, K. M. Shokat, A. Weiss, A sharp T-cell antigen receptor signaling threshold for T-
1053 cell proliferation, *Proceedings of the National Academy of Sciences* **111**, E3679–88 (2014).
- 1054 47. F. H. W. Shand, S. Ueha, M. Otsuji, S. S. Koid, S. Shichino, T. Tsukui, M. Kosugi-
1055 Kanaya, J. Abe, M. Tomura, J. Ziogas, K. Matsushima, Tracking of intertissue migration
1056 reveals the origins of tumor-infiltrating monocytes, *Proceedings of the National Academy of*
1057 *Sciences* **111**, 7771–7776 (2014).
- 1058 48. G. Hajishengallis, T. Chavakis, Local and systemic mechanisms linking periodontal
1059 disease and inflammatory comorbidities, *Nat Rev Immunol* (2021), doi:10.1038/s41577-020-
1060 00488-6.
- 1061 49. M. B. Buechler, K.-W. Kim, E. J. Onufer, J. W. Williams, C. C. Little, C. X. Dominguez, Q.
1062 Li, W. Sandoval, J. E. Cooper, C. A. Harris, M. R. Junttila, G. J. Randolph, S. J. Turley, A
1063 Stromal Niche Defined by Expression of the Transcription Factor WT1 Mediates
1064 Programming and Homeostasis of Cavity-Resident Macrophages, *Immunity* **51**, 119–130.e5
1065 (2019).
- 1066 50. M. Kursar, K. Bonhagen, A. Köhler, T. Kamradt, S. H. E. Kaufmann, H.-W. Mittrücker,
1067 Organ-specific CD4+ T cell response during *Listeria monocytogenes* infection, *J. Immunol.*
1068 **168**, 6382–6387 (2002).
- 1069 51. Y. Ando, O. Murai, Y. Kuwajima, S. Furukawa, D. Sasaki, Y. Okawa, T. Yaegashi, H.
1070 Miura, A. Fujimura, Lymphatic architecture of the human gingival interdental papilla,
1071 *Lymphology* **44**, 146–154 (2011).
- 1072 52. J. Barreto de Albuquerque, D. Silva dos Santos, J. V. Stein, J. de Meis, Oral Versus
1073 Intra-gastric Inoculation: Similar Pathways of *Trypanosoma cruzi* Experimental Infection?
1074 From Target Tissues, Parasite Evasion, and Immune Response, *Front. Immun.* **9**, 375–9
1075 (2018).
- 1076 53. D. Silva dos Santos, J. Barreto de Albuquerque, B. Guerra, O. C. Moreira, L. R. Berbert,
1077 M. T. Ramos, B. A. S. Mascarenhas, C. Britto, A. Morrot, D. M. Serra Villa-Verde, L. R.
1078 Garzoni, W. Savino, V. Cotta-de-Almeida, J. de Meis, Unraveling Chagas disease
1079 transmission through the oral route: Gateways to *Trypanosoma cruzi* infection and target
1080 tissues, *PLoS Negl Trop Dis* **11**, e0005507 (2017).
- 1081 54. R. Pabst, Mucosal vaccination by the intranasal route. Nose-associated lymphoid tissue
1082 (NALT)-Structure, function and species differences, *Vaccine* **33**, 4406–4413 (2015).
- 1083 55. H. Sigmundsdottir, E. C. Butcher, Environmental cues, dendritic cells and the
1084 programming of tissue-selective lymphocyte trafficking, *Nat Immunol* **9**, 981–987 (2008).
- 1085 56. R. Molenaar, M. Knippenberg, G. Goverse, B. J. Olivier, A. F. de Vos, T. O’Toole, R. E.
1086 Mebius, Expression of retinaldehyde dehydrogenase enzymes in mucosal dendritic cells and
1087 gut-draining lymph node stromal cells is controlled by dietary vitamin A, *The Journal of*
1088 *Immunology* **186**, 1934–1942 (2011).
- 1089 57. B. Johansson-Lindbom, M. Svensson, O. Pabst, C. Palmqvist, G. Márquez, R. Förster,
1090 W. W. Agace, Functional specialization of gut CD103+ dendritic cells in the regulation of
1091 tissue-selective T cell homing, *J. Exp. Med.* **202**, 1063–1073 (2005).

- 1092 58. Z. F. H. M. Boonman, G. J. D. van Mierlo, M. F. Fransen, K. L. M. C. Franken, R.
1093 Offringa, C. J. M. Melief, M. J. Jager, R. E. M. Toes, Intraocular tumor antigen drains
1094 specifically to submandibular lymph nodes, resulting in an abortive cytotoxic T cell reaction,
1095 *J. Immunol.* **172**, 1567–1574 (2004).
- 1096 59. Q. Ma, Y. Decker, A. Müller, B. V. Ineichen, S. T. Proulx, Clearance of cerebrospinal fluid
1097 from the sacral spine through lymphatic vessels, *Journal of Experimental Medicine* **216**,
1098 2492–2502 (2019).
- 1099 60. A. Rashidi, M. Ebadi, D. J. Weisdorf, M. Costalonga, C. Staley, No evidence for
1100 colonization of oral bacteria in the distal gut in healthy adults, *Proceedings of the National*
1101 *Academy of Sciences* **118** (2021), doi:10.1073/pnas.2114152118.
- 1102 61. A. T. Tan, M. Linster, C. W. Tan, N. Le Bert, W. N. Chia, K. Kunasegaran, Y. Zhuang, C.
1103 Y. L. Tham, A. Chia, G. J. D. Smith, B. Young, S. Kalimuddin, J. G. H. Low, D. Lye, L.-F.
1104 Wang, A. Bertoletti, Early induction of functional SARS-CoV-2-specific T cells associates with
1105 rapid viral clearance and mild disease in COVID-19 patients, *CellReports* **34**, 108728 (2021).
- 1106 62. V. Oberhardt, H. Luxenburger, J. Kemming, I. Schulien, K. Ciminski, S. Giese, B.
1107 Csernalabics, J. Lang-Meli, I. Janowska, J. Staniek, K. Wild, K. Basho, M. S. Marinescu, J.
1108 Fuchs, F. Topfstedt, A. Janda, O. Sogukpinar, H. Hilger, K. Stete, F. Emmerich, B. Bengsch,
1109 C. F. Waller, S. Rieg, Sagar, T. Boettler, K. Zoldan, G. Kochs, M. Schwemmle, M. Rizzi, R.
1110 Thimme, C. Neumann-Haefelin, M. Hofmann, Rapid and stable mobilization of CD8+ T cells
1111 by SARS-CoV-2 mRNA vaccine, *Nature* **597**, 268–273 (2021).
- 1112 63. R. Forster, A. Schubel, D. Breitfeld, E. Kremmer, I. Renner-Müller, E. Wolf, M. Lipp,
1113 CCR7 coordinates the primary immune response by establishing functional
1114 microenvironments in secondary lymphoid organs, *Cell* **99**, 23–33 (1999).
- 1115 64. B. C. Schaefer, M. L. Schaefer, J. W. Kappler, P. Marrack, R. M. Kedl, Observation of
1116 antigen-dependent CD8+ T-cell/ dendritic cell interactions in vivo, *Cell Immunol* **214**, 110–
1117 122 (2001).
- 1118 65. A. C. Kirby, M. C. Coles, P. M. Kaye, Alveolar Macrophages Transport Pathogens to
1119 Lung Draining Lymph Nodes, *J. Immunol.* **183**, 1983–1989 (2009).
- 1120 66. L. Madisen, T. A. Zwingman, S. M. Sunkin, S. W. Oh, H. A. Zariwala, H. Gu, L. L. Ng, R.
1121 D. Palmiter, M. J. Hawrylycz, A. R. Jones, E. S. Lein, H. Zeng, A robust and high-throughput
1122 Cre reporting and characterization system for the whole mouse brain, *Nature Neuroscience*
1123 **13**, 133–140 (2010).
- 1124 67. W. N. de Vries, L. T. Binns, K. S. Fancher, J. Dean, R. Moore, R. Kemler, B. B. Knowles,
1125 Expression of Cre recombinase in mouse oocytes: a means to study maternal effect genes,
1126 *genesis* **26**, 110–112 (2000).
- 1127 68. X. Ficht, N. Ruef, B. Stolp, G. P. B. Samson, F. Moalli, N. Page, D. Merkler, B. J. Nichols,
1128 A. Diz-Muñoz, D. F. Legler, V. Niggli, J. V. Stein, In Vivo Function of the Lipid Raft Protein
1129 Flotillin-1 during CD8+ T Cell-Mediated Host Surveillance, *The Journal of Immunology*,
1130 ji1900075 (2019).
- 1131 69. M. E. Abrams, K. A. Johnson, S. S. Perelman, L.-S. Zhang, S. Endapally, K. B. Mar, B.
1132 M. Thompson, J. G. McDonald, J. W. Schoggins, A. Radhakrishnan, N. M. Alto, Oxysterols
1133 provide innate immunity to bacterial infection by mobilizing cell surface accessible
1134 cholesterol, *Nat Microbiol* **5**, 929–942 (2020).

- 1135 70. J. Barreto de Albuquerque, D. Silva dos Santos, A. R. Pérez, L. R. Berbert, E. de
1136 Santana-van-Vliet, D. A. Farias-de-Oliveira, O. C. Moreira, E. Roggero, C. E. de Carvalho-
1137 Pinto, J. Jurberg, V. Cotta-de-Almeida, O. Bottasso, W. Savino, J. de Meis, Trypanosoma
1138 cruzi Infection through the Oral Route Promotes a Severe Infection in Mice: New Disease
1139 Form from an Old Infection? *PLoS Negl Trop Dis* **9**, e0003849 (2015).
- 1140 71. P. A. Romagnoli, H. H. Fu, Z. Qiu, C. Khairallah, Q. M. Pham, L. Puddington, K. M.
1141 Khanna, L. Lefrancois, B. S. Sheridan, Differentiation of distinct long-lived memory CD4 T
1142 cells in intestinal tissues after oral *Listeria monocytogenes* infection, *Mucosal Immunol* **10**,
1143 520–530 (2017).
- 1144 72. T. R. Mempel, M. L. Scimone, J. R. Mora, U. H. von Andrian, In vivo imaging of leukocyte
1145 trafficking in blood vessels and tissues, *Curr Opin Immunol* **16**, 406–417 (2004).
- 1146 73. M. Vladymyrov, J. Abe, F. Moalli, J. V. Stein, A. Ariga, Real-time tissue offset correction
1147 system for intravital multiphoton microscopy, *Journal of Immunological Methods* **438**, 35–41
1148 (2016).
- 1149 74. N. Dutzan, L. Abusleme, J. E. Konkel, N. M. Moutsopoulos, Isolation, Characterization
1150 and Functional Examination of the Gingival Immune Cell Network, *J Vis Exp*, 53736 (2016).
- 1151 75. S. Muller, M. Buhler-Jungo, C. Mueller, Intestinal intraepithelial lymphocytes exert potent
1152 protective cytotoxic activity during an acute virus infection, *J. Immunol.* **164**, 1986–1994
1153 (2000).
- 1154 76. R. C. Team, *R: A Language and Environment for Statistical Computing*, Vienna, Austria.
1155 (2016) (available at <https://www.R-project.org/>).
- 1156 77. D. J. McCarthy, K. R. Campbell, A. T. L. Lun, Q. F. Wills, Scater: pre-processing, quality
1157 control, normalization and visualization of single-cell RNA-seq data in R, *Bioinformatics* **33**,
1158 1179–1186 (2017).
- 1159 78. A. T. L. Lun, K. Bach, J. C. Marioni, Pooling across cells to normalize single-cell RNA
1160 sequencing data with many zero counts, *Genome Biology* **17**, 75–14 (2016).
- 1161 79. A. T. L. Lun, D. J. McCarthy, J. C. Marioni, A step-by-step workflow for low-level analysis
1162 of single-cell RNA-seq data with Bioconductor, *F1000Res* **5**, 2122 (2016).
- 1163 80. T. Stuart, A. Butler, P. Hoffman, C. Hafemeister, E. Papalexi, W. M. Mauck, Y. Hao, M.
1164 Stoeckius, P. Smibert, R. Satija, Comprehensive Integration of Single-Cell Data, *Cell* **177**,
1165 1888–1902.e21 (2019).
- 1166 81. L. Zappia, A. Oshlack, Clustering trees: a visualization for evaluating clusterings at
1167 multiple resolutions, *Gigascience* **7** (2018), doi:10.1093/gigascience/giy083.
- 1168

1169 **Figure legends**

1170 **Figure 1. Lm uptake into oral cavity leads to rapid bacterial accumulation in mandLN.**

1171 **A.** Drainage of a tracer injected into the gingiva to mandLN (arrowheads). **B.** Overview of
1172 lymphatic vessel network in gingiva of Prox1-GFP reporter mouse. **C.** 2PM reconstruction of
1173 lymphatic network in gingiva surrounding mandibular incisors. Scale bar, 20 μ m. **D.** Overview
1174 of lymphatic vessels between mandibular incisors and mandLN of Prox1-GFP reporter
1175 mouse. MM, masseter muscle; mandLN, mandibular lymph node; SLG, sublingual salivary
1176 gland; SMG, submandibular salivary gland. **E.** Experimental layout. **F.** Lm-OVA CFU per
1177 lymphoid organ after intraoral (i.o.) *versus* intravenous (i.v.) Lm infection. Lines depict
1178 median, and dotted line indicates limit of detection. **G.** Lymphoid organ cellularity during i.o.
1179 and i.v. Lm-OVA infection. **H.** CFU counts in mandLN after i.o. infection of Lm-OVA or Lm-
1180 InIA^m. **I.** Lm-OVA CFU counts in mandLN after i.o. infection of WT or CCR7^{-/-} mice. **J.** Lm-
1181 GFP accumulation (arrowheads) at distinct depths from mandLN capsule after i.o. infection.
1182 SHG, second harmonic generation. Scale bar, 40 μ m. Data in F and G are from 2-3
1183 independent experiments with each 2-3 mice/time point. Data in G were analyzed using a
1184 Kruskal-Wallis test against “d 0”. Data in H and I are pooled from 2-3 independent
1185 experiments and analyzed using a Mann-Whitney test. *, p < 0.05; **, p < 0.01; ***, p < 0.001.

1186

1187 **Figure 2. Visualization of CD8⁺ T cell dynamics in mandLN after oral Lm uptake. A.**

1188 Experimental layout. **B.** Confocal images of mandLN sections after i.o. Lm-OVA
1189 administration. Scale bar, 200 (top) and 20 (bottom) μ m. **C.** Representative 2PM images of
1190 infected mandLN of CD11c-YFP host containing OT-I cells and polyclonal T cells at d 2 p.i..
1191 Left panel shows OT-I clusters around CD11⁺ cells (dotted line), right panel shows overlaid
1192 tracks of OT-I (yellow) and polyclonal CD8⁺ T cells (blue). Scale bar, 20 μ m. **D-F.**
1193 Quantification of imaging data. Track speeds (D), arrest coefficient (E), and corrected track
1194 straightness (F). Lines in D and E depict median. Data in D were analyzed using ANOVA
1195 with Sidak’s multiple comparison test, in E using Kruskal-Wallis with Dunn’s multiple

1196 comparison test and in F using Mann-Whitney test. Data are representative (B, C) or pooled
1197 (D-F) from at least two independent experiments. *, $p < 0.05$; **, $p < 0.01$; ***, $p < 0.001$.

1198

1199 **Figure 3. MandLN DC trigger CD8⁺ T cell activation.** **A.** Flow cytometry plot of CD103⁺
1200 and CD103⁻ DC. **B, C.** CD80 (B) and CD86 (C) expression and MFI on CD103⁺ and CD103⁻
1201 DC before and after Lm infection. **D.** Experimental set up for *in vitro* CD8⁺ T cell activation by
1202 mandLN DC. **E, F.** Representative flow cytometry plots (E) and quantification (F) of Nur77-
1203 GFP, CD69 and CD25 expression, and proliferation. Data in B and C are from one of two
1204 independent experiments with 4 mice/group and analyzed using an unpaired t-test. Data in F
1205 are pooled from 2 independent experiments with 1-4 replicates each and analyzed with one-
1206 way ANOVA with Dunnett's multiple comparison test against "- DC" (no DC). *, $p < 0.05$; ***,
1207 $p < 0.001$.

1208

1209 **Figure 4. Oral Lm exposure triggers rapid CD8⁺ T cell effector generation in mandLN.**
1210 **A.** Experimental layout. **B, C.** CD69 (B) and CD25 (C) expression in OT-I cells isolated from
1211 mandLN, spleen and MLN after i.o. Lm-OVA infection. **D.** Representative flow cytometry
1212 plots of OT-I T cell proliferation after i.o. Lm-OVA infection. Numbers indicate percent of
1213 proliferated cells. **E.** OT-I proliferation in mandLN, spleen and MLN after i.o. Lm infection. **F.**
1214 OT-I cell number in lymphoid organs after i.o. and i.v. infection. Numbers depict fold increase
1215 in median "d 3" OT-I cell numbers over "d 0". **G-I.** Examples of flow cytometry plots (G) and
1216 pie charts showing the proportion of OT-I populations based on CD44/CD62L (H) and
1217 KLRG1/CD127 (I) expression on d 5 and 30 following i.o. and i.v. infections. Lines in B, C, E,
1218 and F depict median. Data in B and C are pooled from 2-5 experiments per time point with 3
1219 mice per experiment and analyzed by ANOVA. Data in E are pooled from 2 independent
1220 experiments. Data in F, H and I are pooled from 2-3 independent experiments with each 2-3
1221 mice/group/time point and analyzed using a Kruskal-Wallis test against "d 0" (F). *, $p < 0.05$;
1222 **, $p < 0.01$; ***, $p < 0.001$.

1223

1224 **Figure 5. MandLN CD8⁺ T_{EFF} constitute the majority of the early circulating T_{EFF} pool for**
1225 **host protection. A.** Experimental layout of egress blockade. **B.** OT-I cell numbers in
1226 mandLN, spleen and MLN on d 4 and 5 post i.o. Lm-OVA infection in presence or absence of
1227 FTY720. **C.** Experimental layout of photoconversion. **D.** Representative flow cytometry plots
1228 for photoconverted (KikGR-red) and non-photoconverted (KikGR-green) OT-I cells and their
1229 CD44 expression from mice in the presence or absence of Lm-OVA. Numbers depict
1230 percentages. **E.** Numbers of KikGR-red⁺ CD44^{high} OT-I cells per lymphoid organ. **F.**
1231 Experimental layout of target cell killing. **G.** Cell number in lymphoid organs in the presence
1232 or absence of anti-CD62L treatment. **H.** Flow cytometry histograms for unpulsed (U) and
1233 OVA₂₅₇₋₂₆₄-pulsed (P) B cells in the presence or absence of anti-CD62L. **I.** Ratio of OVA₂₅₇₋
1234 ₂₆₄-pulsed and unpulsed B cells in the spleen. **J.** Numbers of OT-I cells in the spleen in the
1235 presence or absence of anti-CD62L. Data in B are pooled from 2 independent experiments
1236 with 3-4 mice each and analyzed using an unpaired t-test. Data in E are pooled from 2
1237 independent experiments with 2-3 mice each. Data in G, I and J are pooled from 2
1238 independent experiments with 3-5 mice/group for presence/absence of anti-CD62L mAb, and
1239 2 independent experiments each with 2 mice/group as controls. Data in G were analyzed
1240 with unpaired t test and Welch`s correction. Data in I and J were analyzed with Mann-
1241 Whitney test. *, p < 0.05; **, p < 0.01; ***, p < 0.001.

1242

1243 **Figure 6. Mand LN T_{EFF} lack expression of signature gut trafficking receptors and**
1244 **home to SLO, lung and OM but not the small intestine. A.** Experimental layout of Lm-
1245 OVA infections. **B-E.** Flow cytometry plots and quantification for adhesion receptors α_L
1246 (CD11a), α_4 (CD49d), β_1 (CD29) and β_7 integrins (B), chemokine receptors CXCR3, CX3CR1
1247 and CXCR6 (C), effector proteins Granzyme B (GzmB), IFN- γ , TNF- α and IL-2 (D) and gut
1248 trafficking receptors $\alpha_4\beta_7$ and CCR9 (E). Black bar indicate gate, grey is FMO. **F.**
1249 Experimental layout of OT-I T_{EFF} adoptive transfer. **G-I.** Ratio of MLN- to spleen-primed OT-I
1250 (G) and mandLN- to spleen-primed OT-I T_{EFF} (H) recovered from each organ. Values are

1251 normalized to the T_{EFF} ratio in recipient spleens. nd, not detected. SMG, submandibular
1252 salivary gland; OM, oral mucosa; SI, small intestine. **I.** Normalized ratio of mandLN- to
1253 spleen-primed OT-I T_{EFF} in lung, OM and small intestine (from data in G). Data in B-D and G-
1254 I are pooled from 2 independent experiments with 4-5 mice each and analyzed using ANOVA
1255 and Tukey post-test. Data in E are representative of two independent experiments. Data in I
1256 were analyzed using Wilcoxon test. *, $p < 0.05$; **, $p < 0.01$; ***, $p < 0.001$.

1257

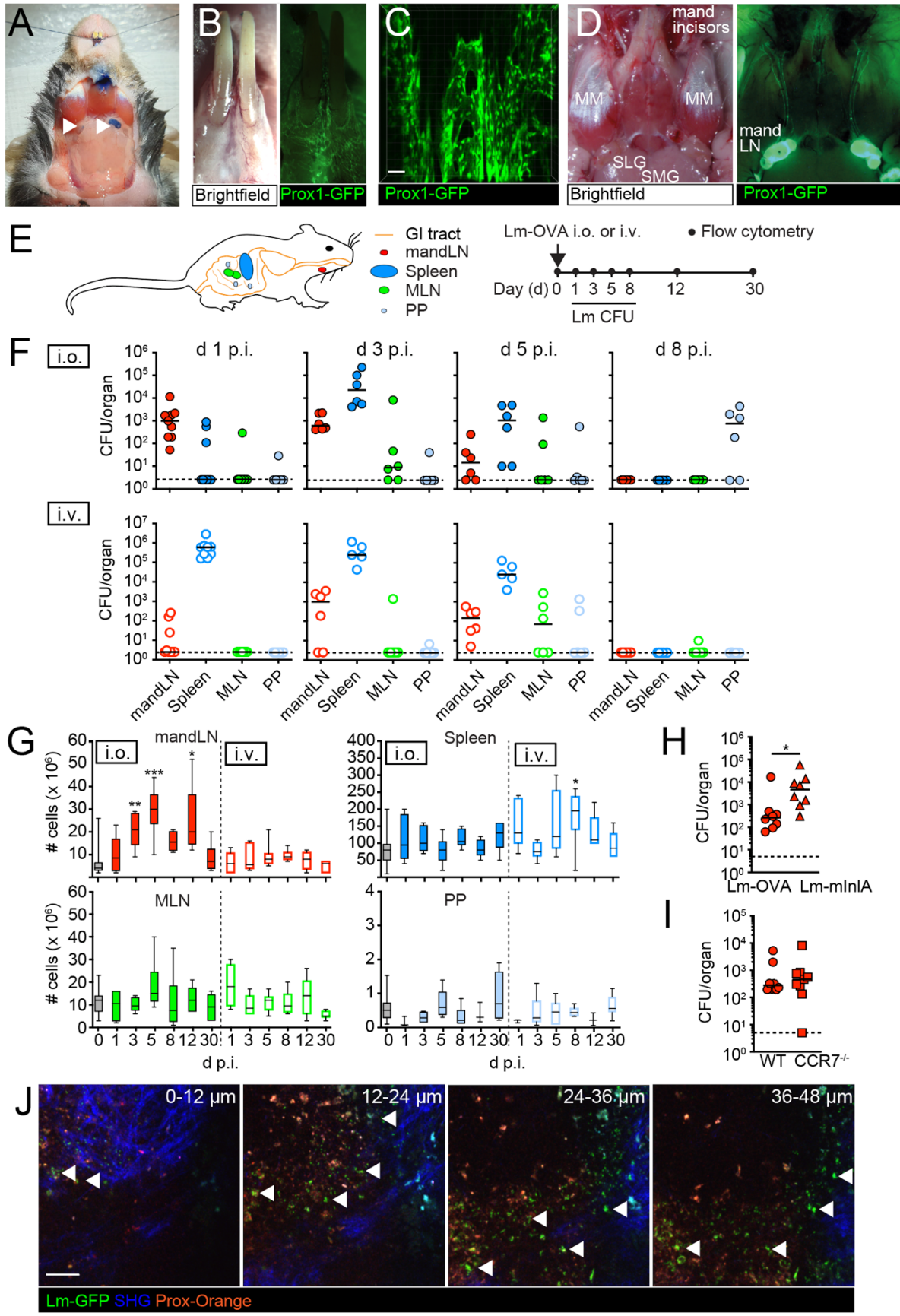
1258 **Figure 7. Low expression of genes for gut-homing imprinting in mandLN stromal cells**

1259 **DC. A.** UMAP clustering of pooled TER119⁻ CD45⁻ stromal cells of MLN, PLN and mandLN
1260 based on scRNAseq data. Numbers indicate individual clusters. **B.** Expression of *Aldh1a1*,
1261 *Aldh1a2*, *Aldh1a3* and *WT1* in MLN (10058 cells), PLN (7750 cells) and mandLN stroma
1262 (4434 cells) based on scRNAseq data. **C.** Expression frequency of *Aldh1a1*, *Aldh1a2*,
1263 *Aldh1a3* and *WT1* in fibroblast-like cells based on data in B. **D.** *Aldh1a1*, *Aldh1a2* and
1264 *Aldh1a3* expression in TER-119⁻ CD45⁻ stromal cells and CD11c⁺ MHC-II⁺ DC isolated from
1265 of MLN, PLN and mandLN assessed by qPCR. Shown are the $2^{-\Delta CT}$ means of duplicates
1266 from two independent experiments (grey and white fill). Bars represent mean.

1267

1268 **Figure 8. MandLN-primed OT-I T_{EFF} reduce systemic Lm burden but do not protect**

1269 **MLN and PP after intragastric infection. A.** Experimental layout. **B.** Lm-OVA CFU in
1270 spleen, MLN and PP after adoptive transfer of spleen-, mandLN- and MLN-primed OT-I T_{EFF} .
1271 Numbers indicate percentage of organs with Lm-OVA CFU above limit of detection (dotted
1272 line). **C.** Graphical summary. Inception of oral pathogen in mandLN leads to a rapid release
1273 of protective CD8⁺ T_{EFF} that preferentially relocate to SLO, lung and OM. CSF, cerebrospinal
1274 fluid; AEC, anterior eye chamber. Created with BioRender.com. Data in B are pooled from 4
1275 independent experiments and analyzed using a Kruskal Wallis test against “no OT-I”. ***, $p <$
1276 0.001.



1277 Figure 1

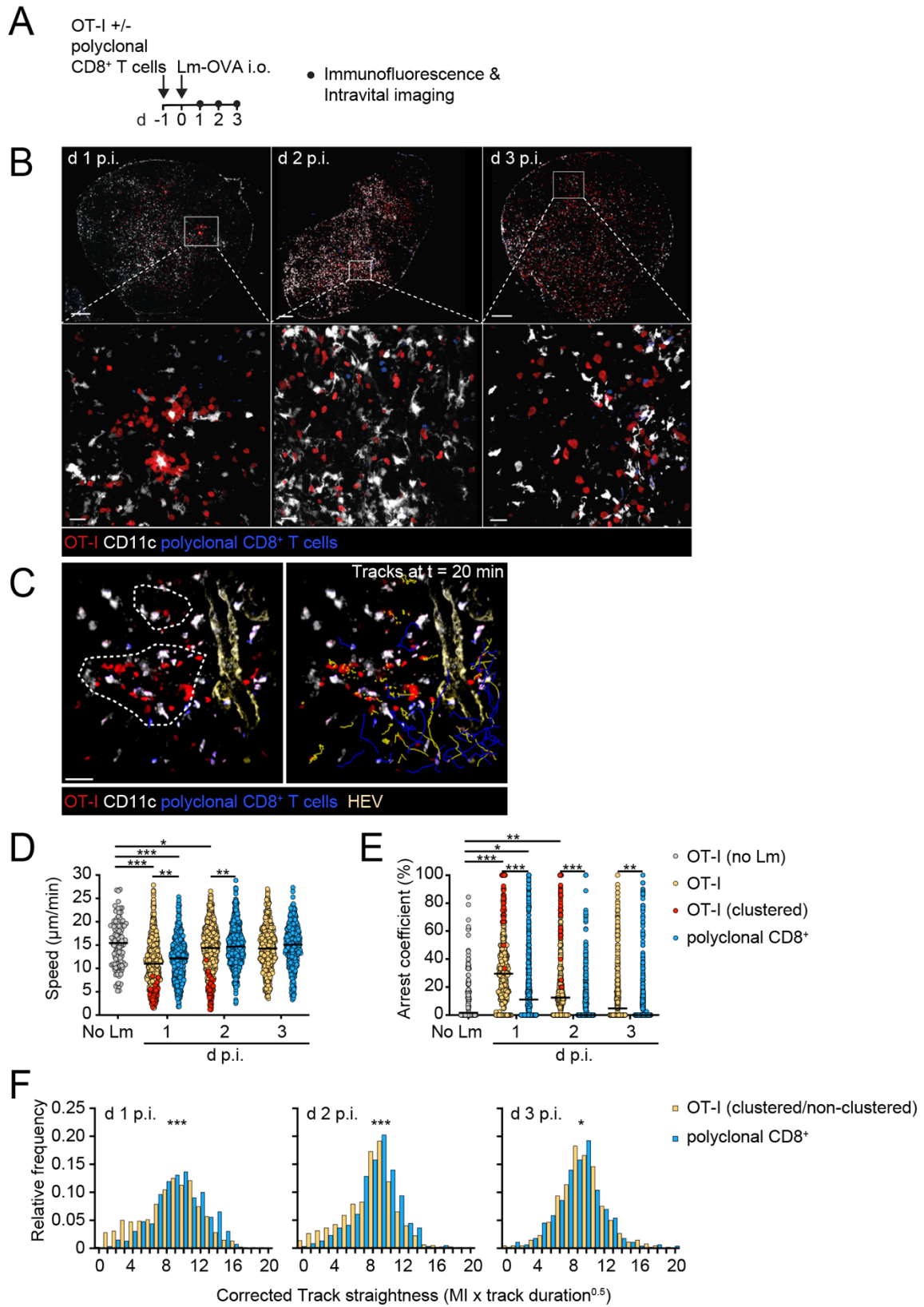


Figure 2

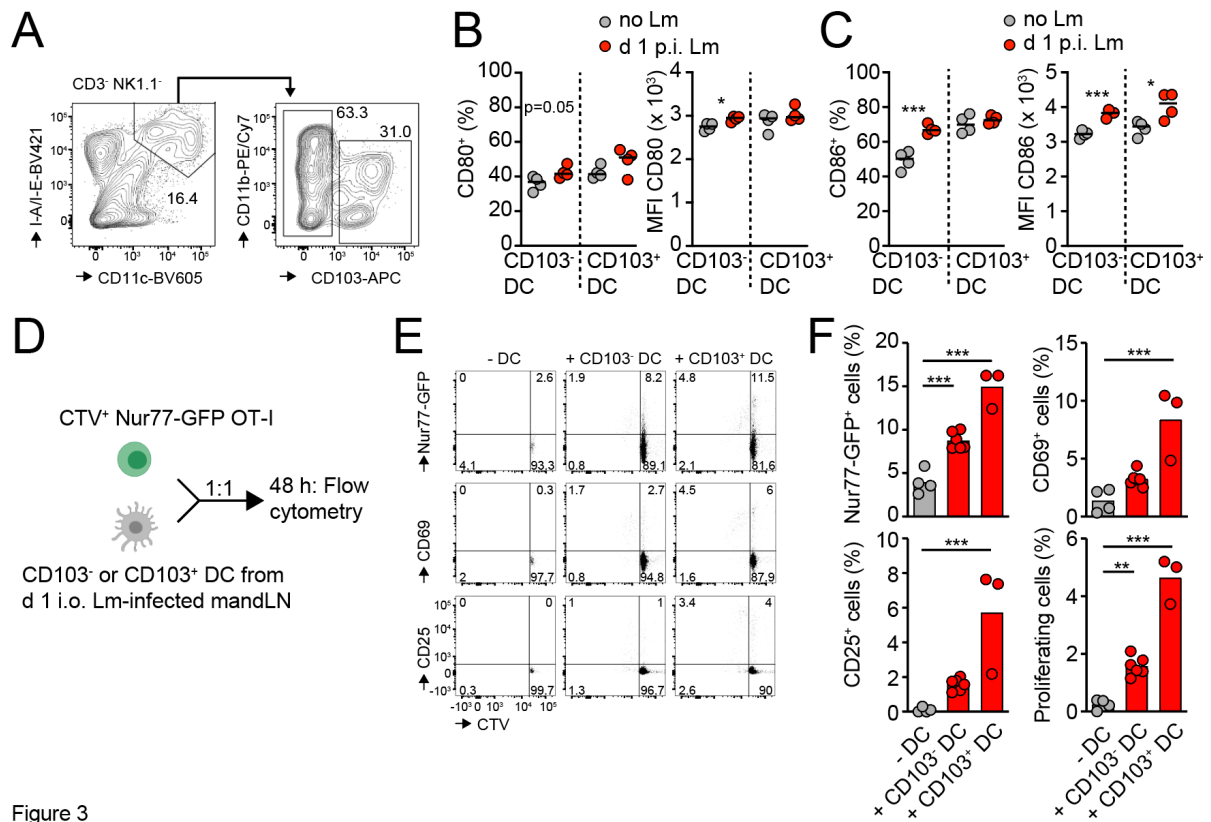


Figure 3

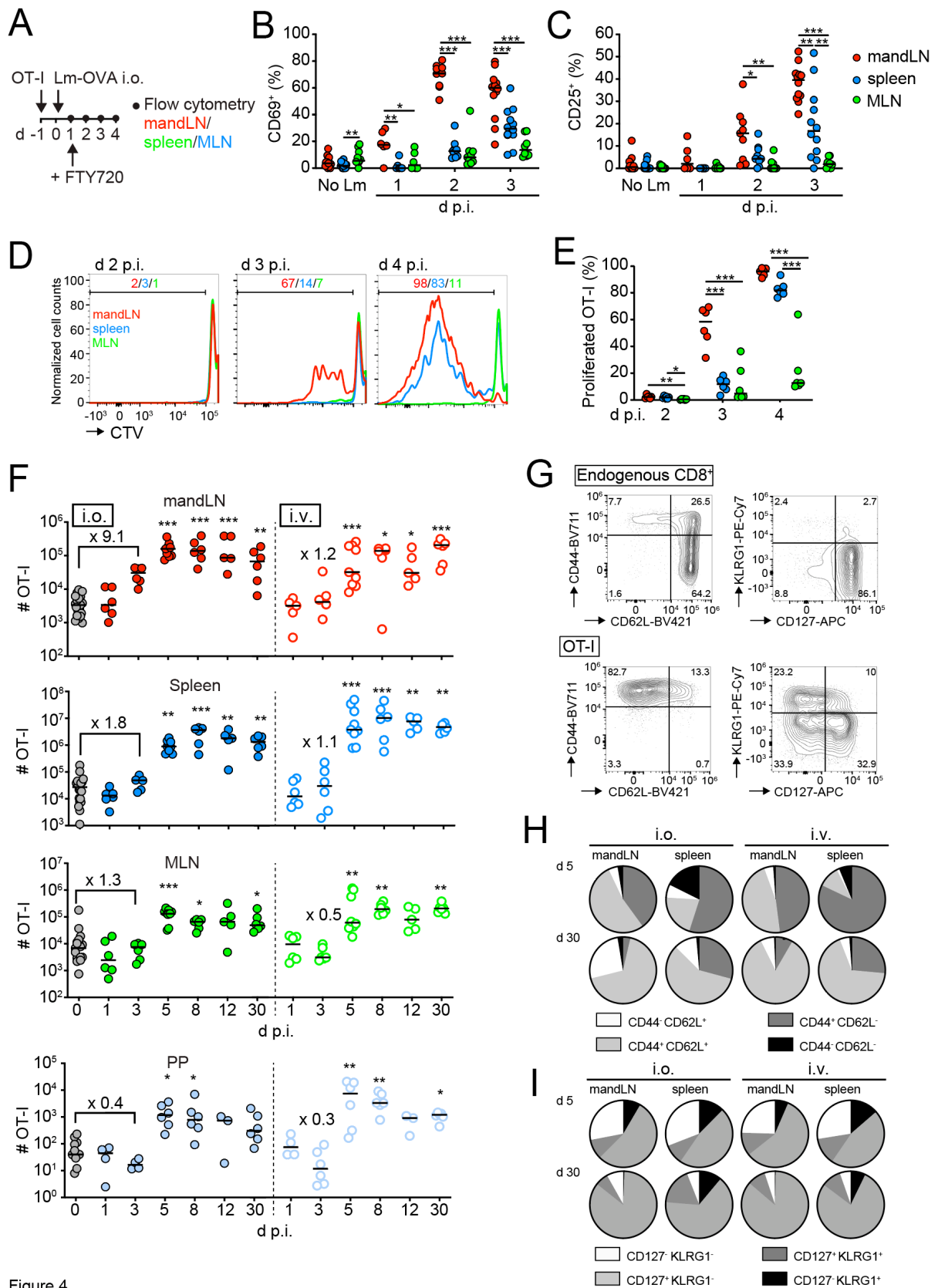


Figure 4

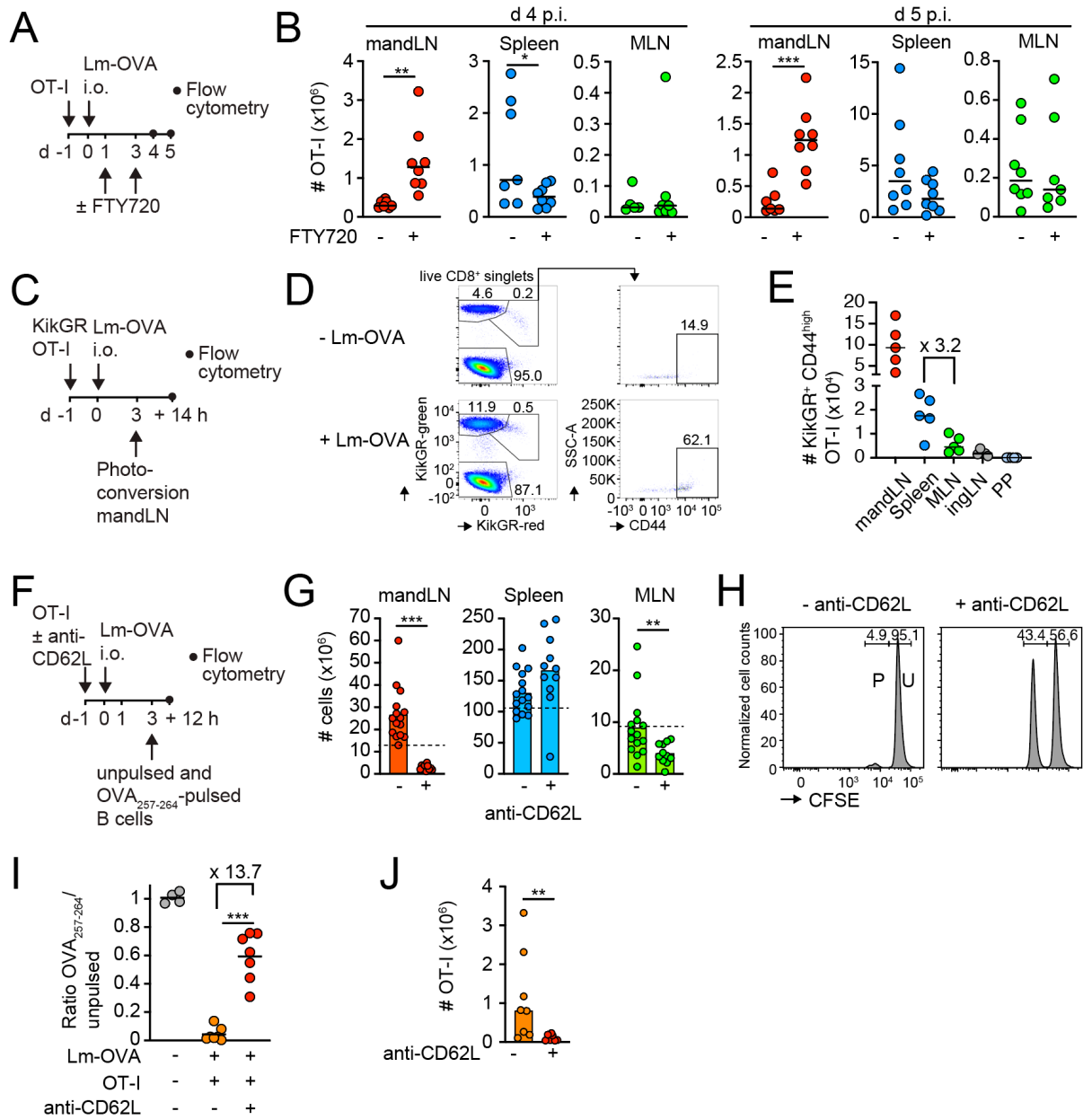


Figure 5

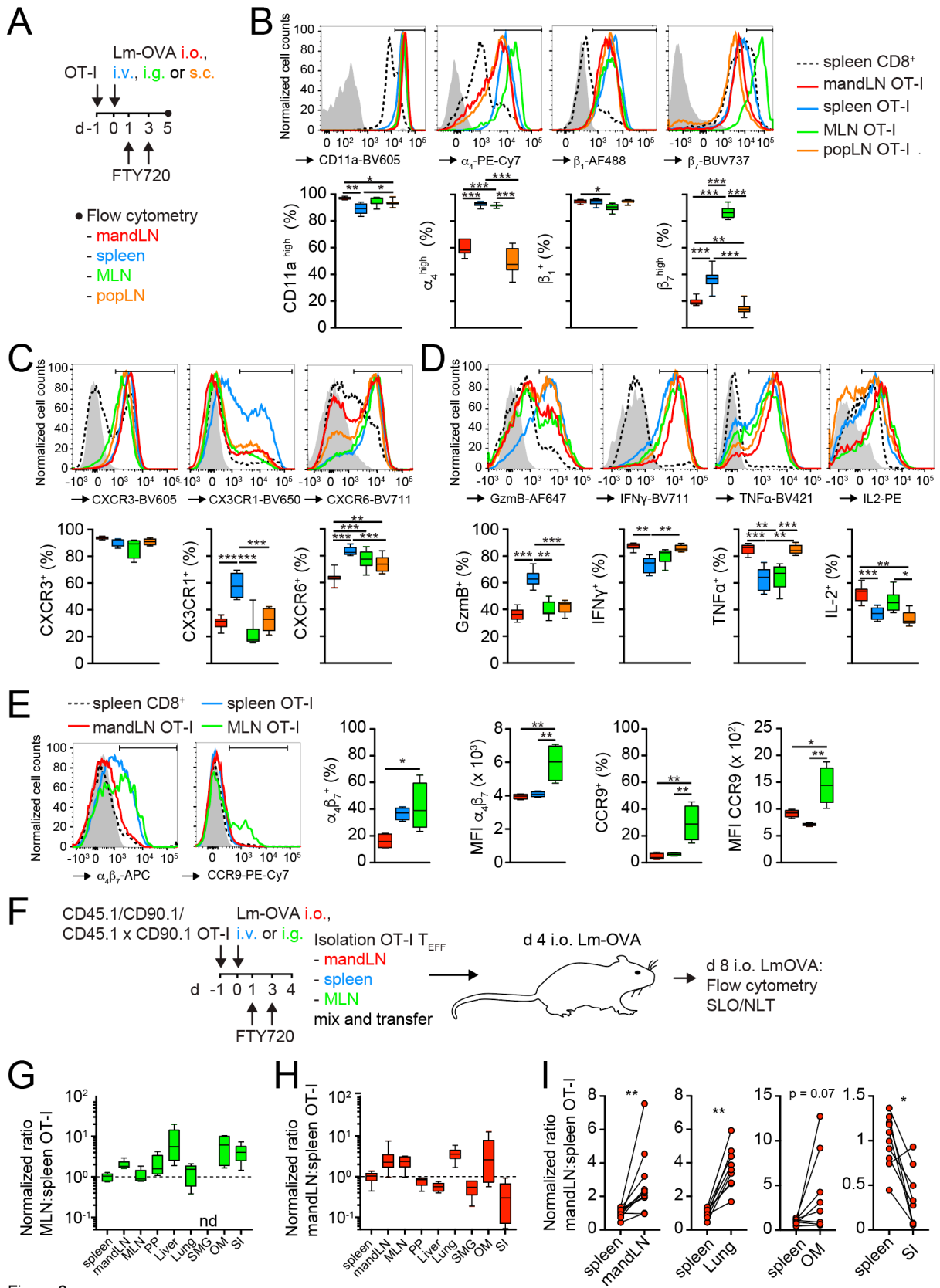


Figure 6

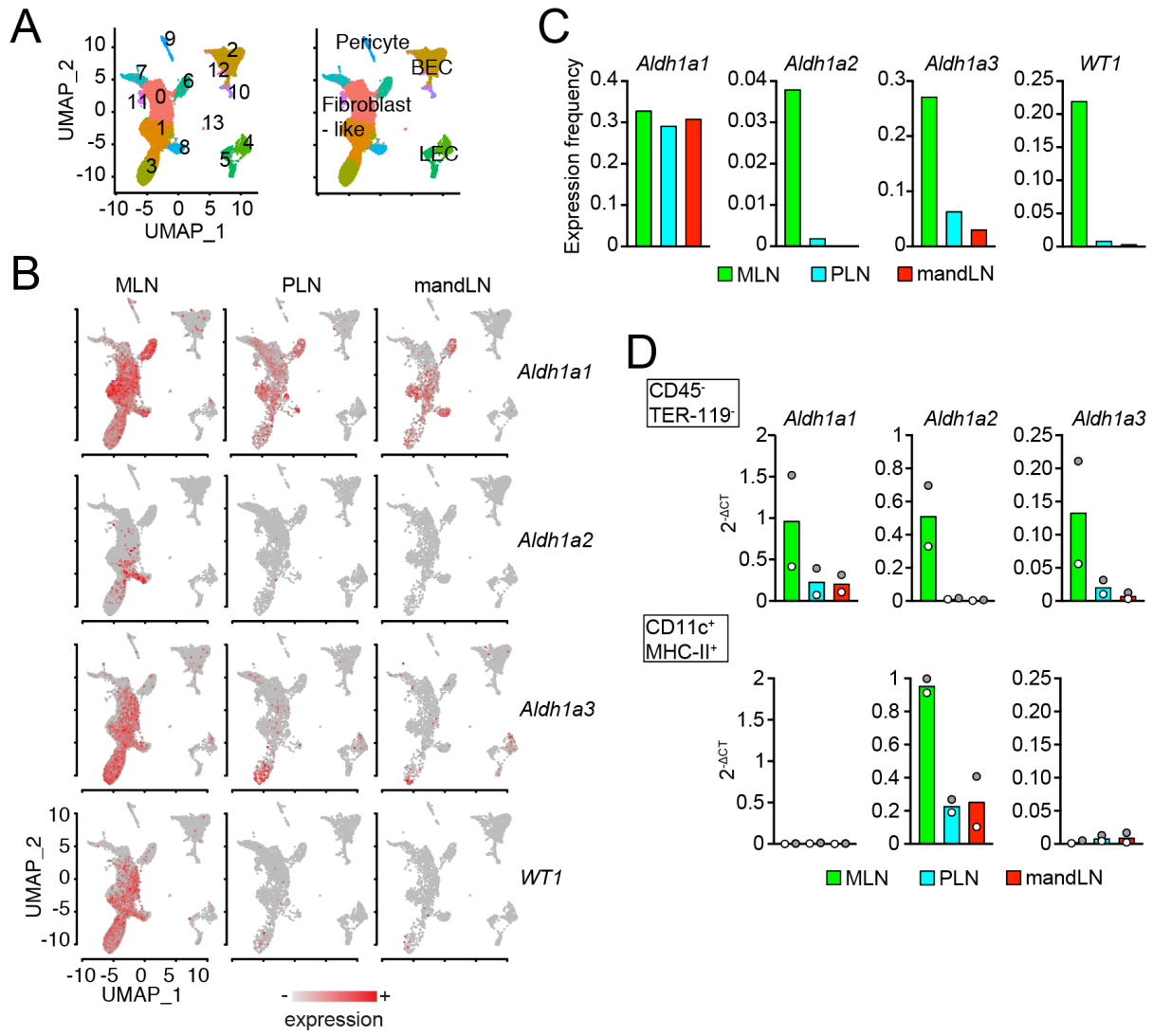


Figure 7

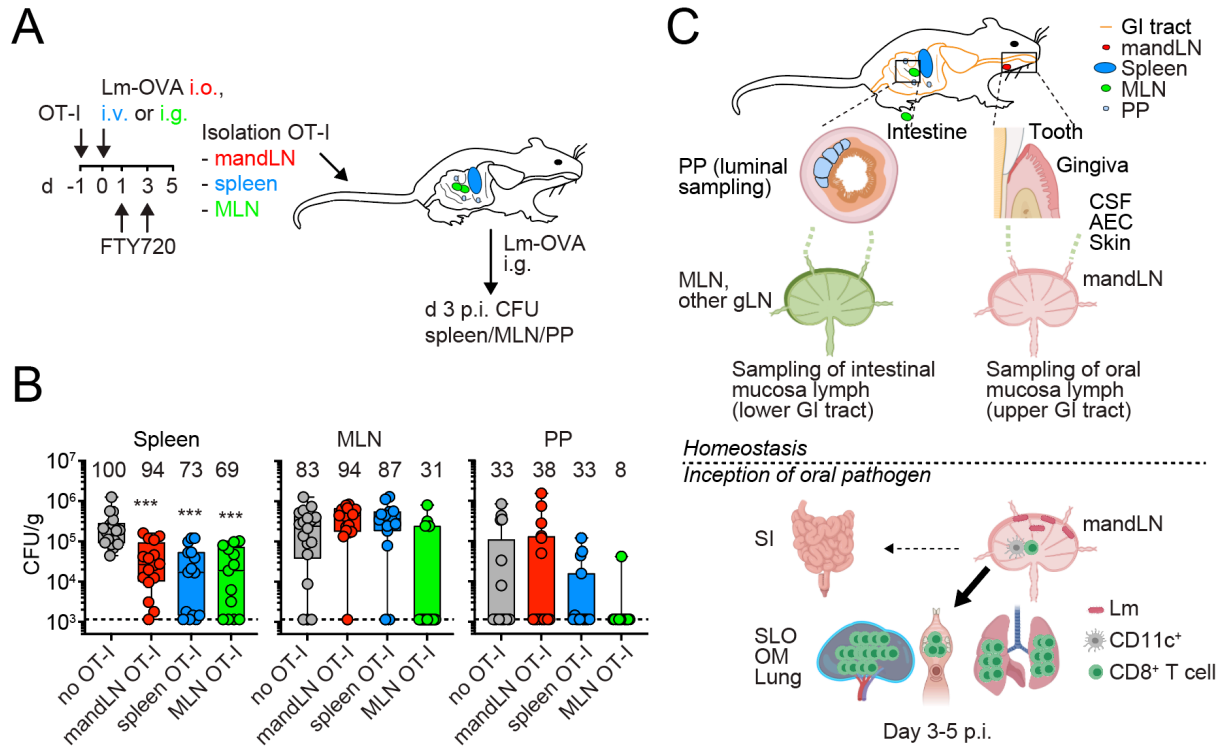


Figure 8

1285 **Supplemental Figure legend**

1286 **Figure S1. A, B.** Surgical setup (left panels) and stereomicroscope images (right panels) of
1287 gingiva (A) and mandLN (B). SMG, submandibular salivary gland.

1288

1289 **Figure S2. Flow cytometry analysis of DC and CD8⁺ T cells. A.** Flow cytometry plots of
1290 migratory (CD11c^{intermediate} MHCII^{high}) and resident (CD11c^{high} MHCII^{intermediate}) DC
1291 classification and expression of CD80 and CD86. Grey shade, FMO. Numbers indicate
1292 percent expressing cells. **B, C.** CD80 (B) and CD86 (C) expression and MFI on migratory
1293 and resident DC. **D.** Gating strategy for CD103⁺ and CD103⁻ DCs and CCR7 expression on
1294 cDC1 (XCR1⁺ SIRPalpha⁻) and cDC2 subsets (XCR1⁻ SIRPalpha⁺) isolated from mandLN.
1295 Lineage markers for exclusion contain anti-NK1.1, TCRβ, CD19 and Ly6C mAbs. Numbers
1296 indicate percentage in gate. **E.** Gating strategy for adoptively transferred OT-I T cells. Data in
1297 B and C are from one of two independent experiments with 4 mice/group, while data in D are
1298 pooled from 2 experiments with 4-6 mice, and analyzed using an unpaired t-test.

1299

1300 **Figure S3. CD8⁺ T cell activation in mandLN occurs over a wide range of Lm inocula**
1301 **and consumption of Lm-contaminated food. A.** Experimental layout for Lm-OVA titration.
1302 **B.** Flow cytometry plots of CD69/CD25 expression and proliferation in mandLN OT-I T cells
1303 on d 3 p.i. after titrating Lm-OVA inoculum. **C-F.** CD69 expression (C), MFI CD69 (D), CD25
1304 expression (E) and proliferation (F) on mandLN OT-I T cells after titrating Lm-OVA inoculum.
1305 Numbers in F depict percent proliferated ± SEM. **G.** MandLN cellularity on d 3 after i.o. Lm-
1306 OVA infection. **H, I.** CD69 expression (H) and MFI CD69 (I) on endogenous mandLN CD8⁺
1307 cells after titrating Lm-OVA inoculum. **J.** Experimental layout for Lm-OVA infection with
1308 ingested contaminated food. **K-N.** Total cellularity (K), number of OT-I (L), CD69 (M) and
1309 CD25 (N) expression in mandLN. Lines in C-I and K-N depict median. Data in C-I are pooled
1310 from 2 independent experiments with each 3 mice/condition and analyzed using a Kruskal-
1311 Wallis test against “no Lm”. Data in K-N are pooled from 2 independent experiments with

1312 each 3-5 mice and analyzed using a Mann-Whitney test. *, $p < 0.05$; **, $p < 0.01$; ***, $p <$
1313 0.001.

1314

1315 **Figure S4. Expression of trafficking and effector markers on orally primed OT-I T cells.**

1316 **A.** Flow cytometry plots and quantification for CLA, α_1 , CCR6, CCR7, CCR8 and CCR10
1317 expression after i.o. Lm infection. Black bar indicate gate, grey shade; FMO. Data are pooled
1318 from 1-2 independent experiments with 2-4 mice each and analyzed using ANOVA and
1319 Tukey post-test. **B. Expression of adhesion receptors, chemokine receptors and effector**
1320 **proteins on mandLN OT-I T cells after ingestion of Lm-contaminated food. Stainings were**
1321 **performed as in Figure 6 and are from one experiment with $n = 5$ mice.** *, $p < 0.05$; **, $p <$
1322 0.01; ***, $p < 0.001$.

1323

1324 **Figure S5. Adoptive transfer of T_{EFF} primed at distinct SLO. A.** Flow cytometry of OT-I
1325 T_{EFF} populations in input. **B.** Gating strategy for transferred T_{EFF} OT-I populations. **C.**
1326 Percentages of mandLN- versus spleen-primed OT-I in spleen, mandLN, MLN, PP, liver,
1327 lung, SMG (submandibular salivary gland), OM and SI after correction for input ratio. **D, E.**
1328 Flow cytometry plots and histograms for CD44 and CD62L (D), as well as KLRG1 and
1329 CD127 expression (E) in endogenous and recovered OT-I T_{EFF} populations. Numbers in A, B
1330 and D indicate percentages. Data in C are pooled from 2 independent experiments.

1331

1332 **Figure S6. Expression of selected genes of interests in stromal cell clusters by**
1333 **scRNAseq.** *Col1a1*, collagen type I alpha 1 chain; *Col1a2*, collagen type I alpha 2 chain;
1334 *Pdpn*, podoplanin; *Cdh5*, VE-cadherin; *Chst4*, Carbohydrate Sulfotransferase 4; *Tnfsf11*,
1335 TNF Superfamily Member 11 (RANKL).

1336

1337 **Figure S7. Differentially expressed genes in T cell zone reticular cells (TRC) cells of**
1338 **mandLN, MLN and PLN.** Differentially expressed genes in CCL21a⁺ TRC (cluster 7) were

1339 analyzed for mandLN *versus* MLN (**A**) and mandLN *versus* PLN (**B**). Pathway enrichment is
1340 expressed as $-\log(P)$.

1341

1342 **Figure S8. Antigen-specific memory CD8⁺ T cells in OM.** Confocal images of tdTom⁺ OT-I
1343 T cells in buccal mucosa, gingiva, palate and tongue on d 72 post oral infection. Scale bar,
1344 40 μm (top) and 5 μm (bottom). Blue, nuclei (DAPI); red, tdTom amplified by anti-RFP
1345 staining.

1346 **Supplementary video legend**

1347 **Video S1.** OT-I motility (red) in mandLN of CD11c-YFP (white) recipients in the absence of
1348 infection. Scale bar, 30 μm ; time in min:s.

1349 **Video S2.** Polyclonal CD8⁺ (blue) and OT-I T cell (red) motility in mandLN of CD11c-YFP
1350 (white) recipients on d 2 post i.o. Lm-OVA infection. HEV are marked in brown. Scale bar, 30
1351 μm ; time in min:s.

1352 **Video S3.** Polyclonal CD8⁺ (blue) and OT-I T cell (red) motility in mandLN of CD11c-YFP
1353 (white) recipients on d 3 post i.o. Lm-OVA infection. HEV are marked in brown. Scale bar, 30
1354 μm ; time in min:s.

1355 **Video S4.** OT-I T cell (red) migration in gingiva in memory phase following i.o. Lm-OVA
1356 infection. SHG, second harmonic generation. Scale bar, 50 μm ; time in min:s.

1357

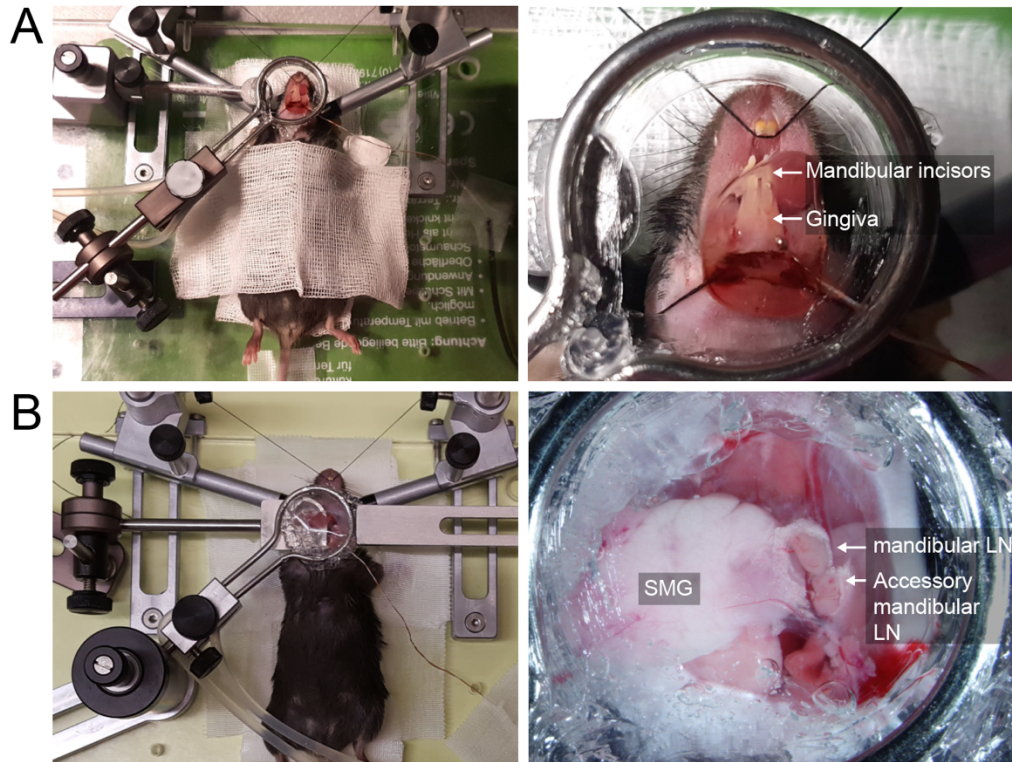


Figure S1

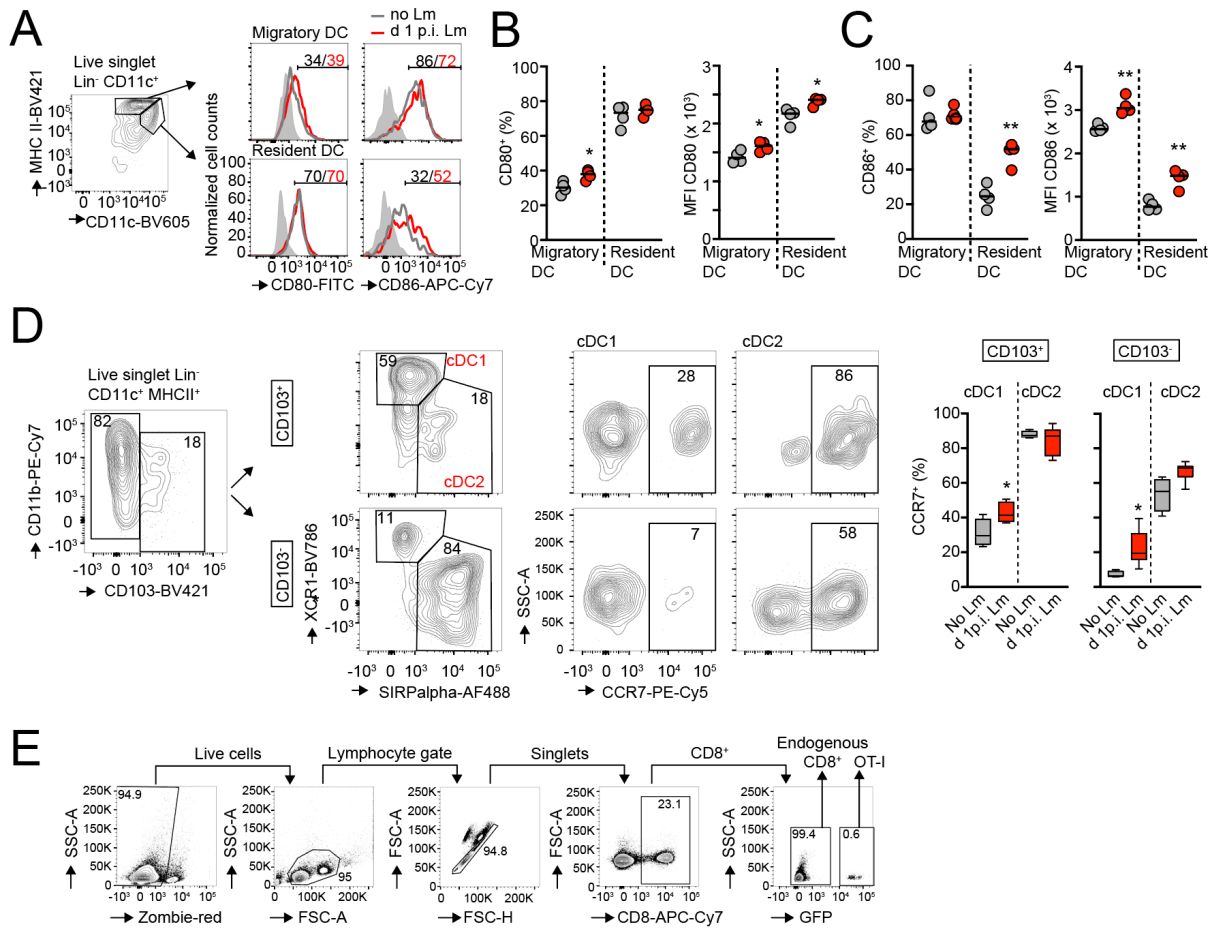


Figure S2

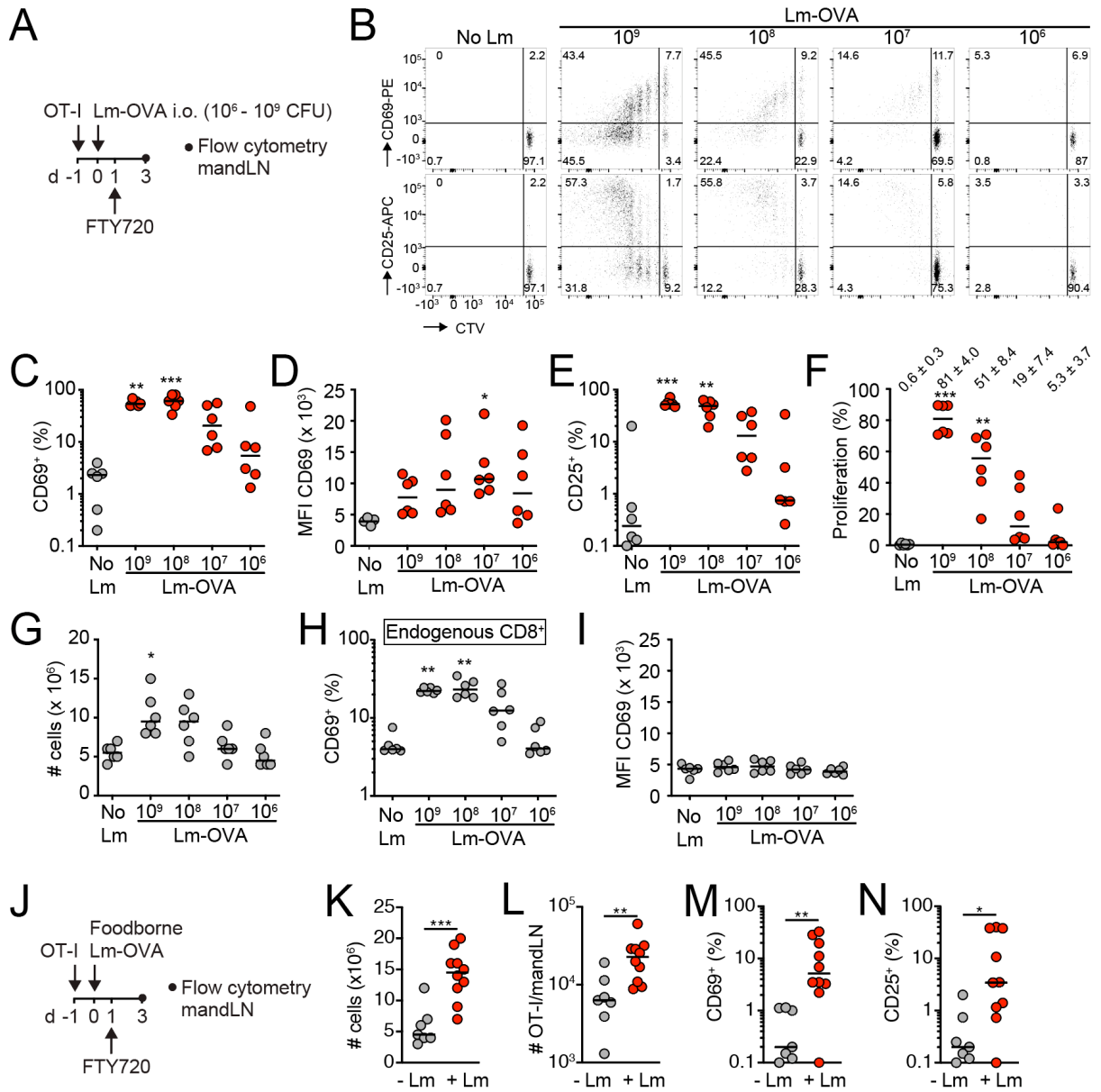


Figure S3

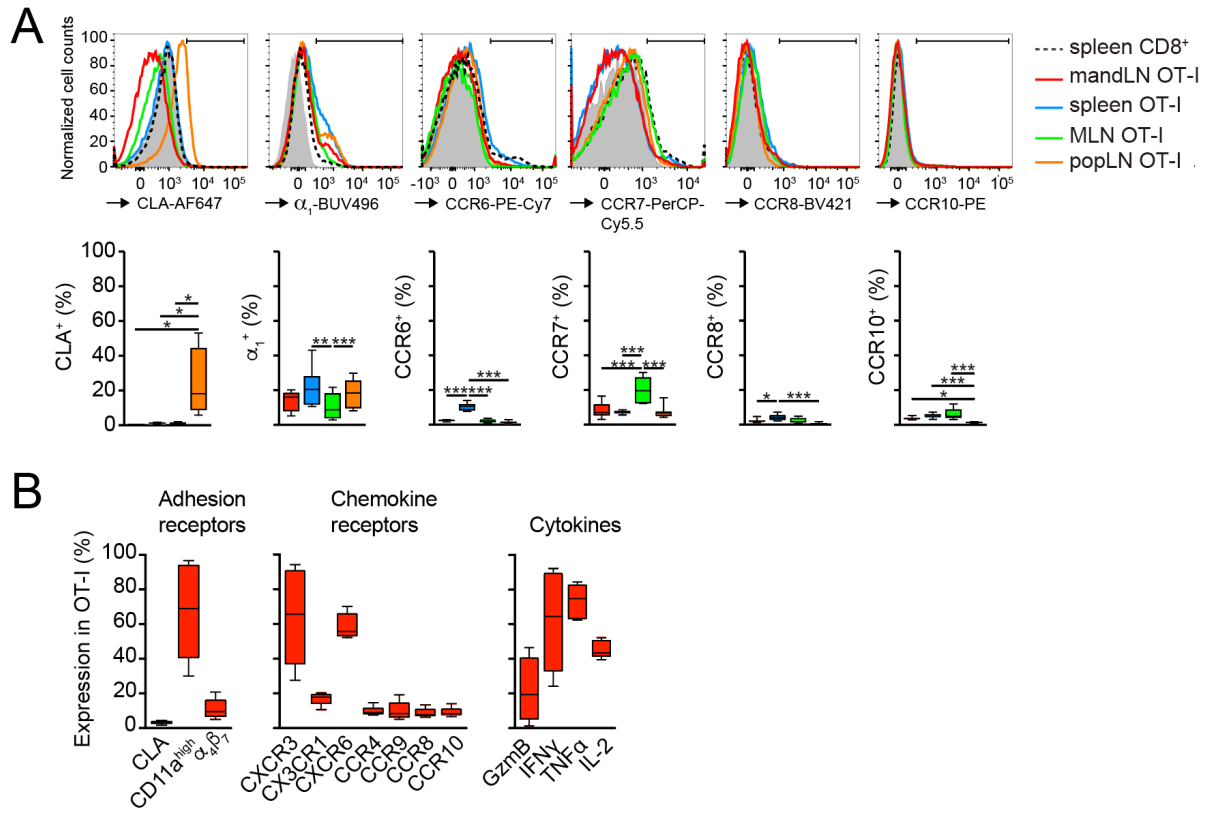


Figure S4

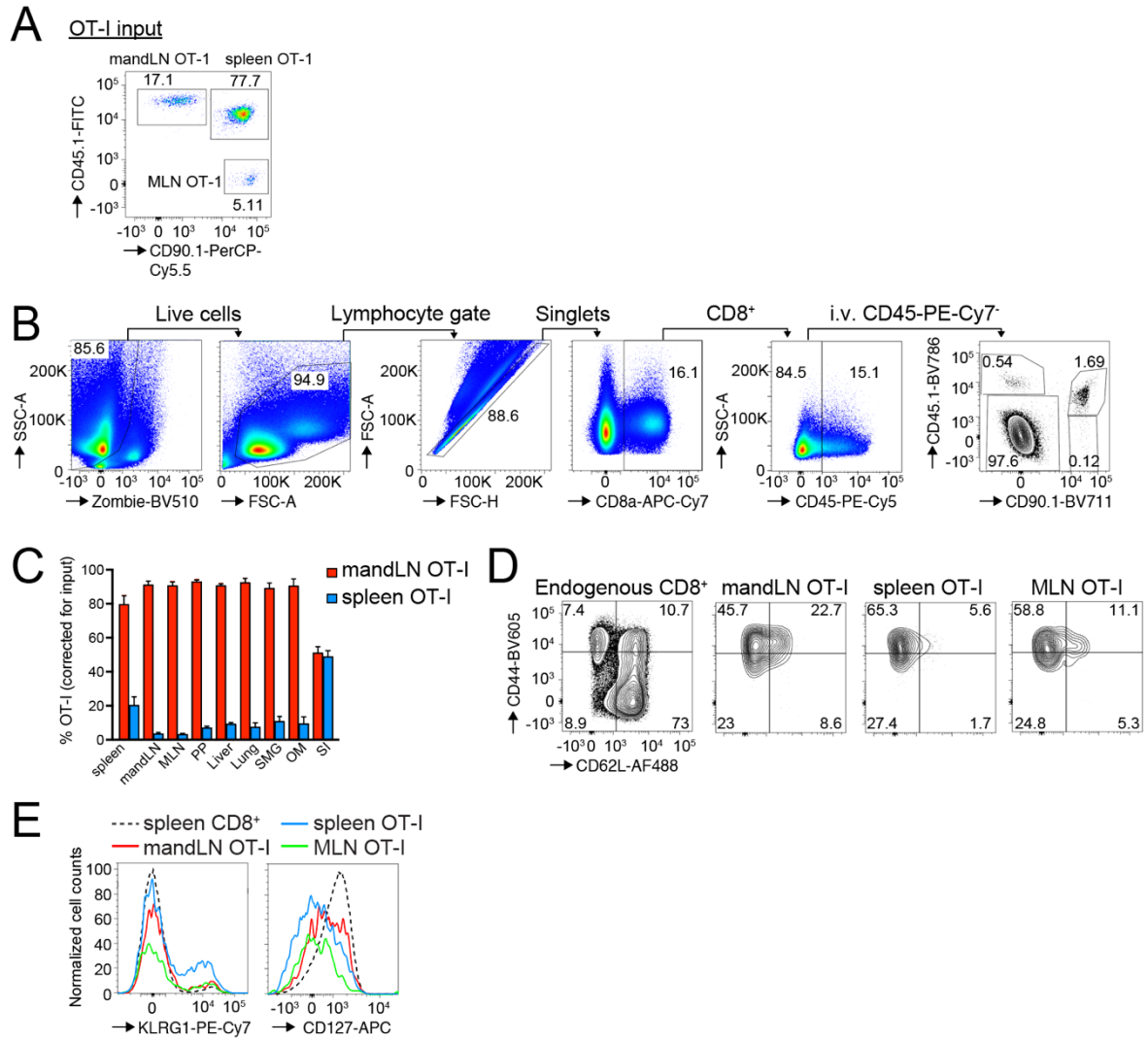


Figure S5

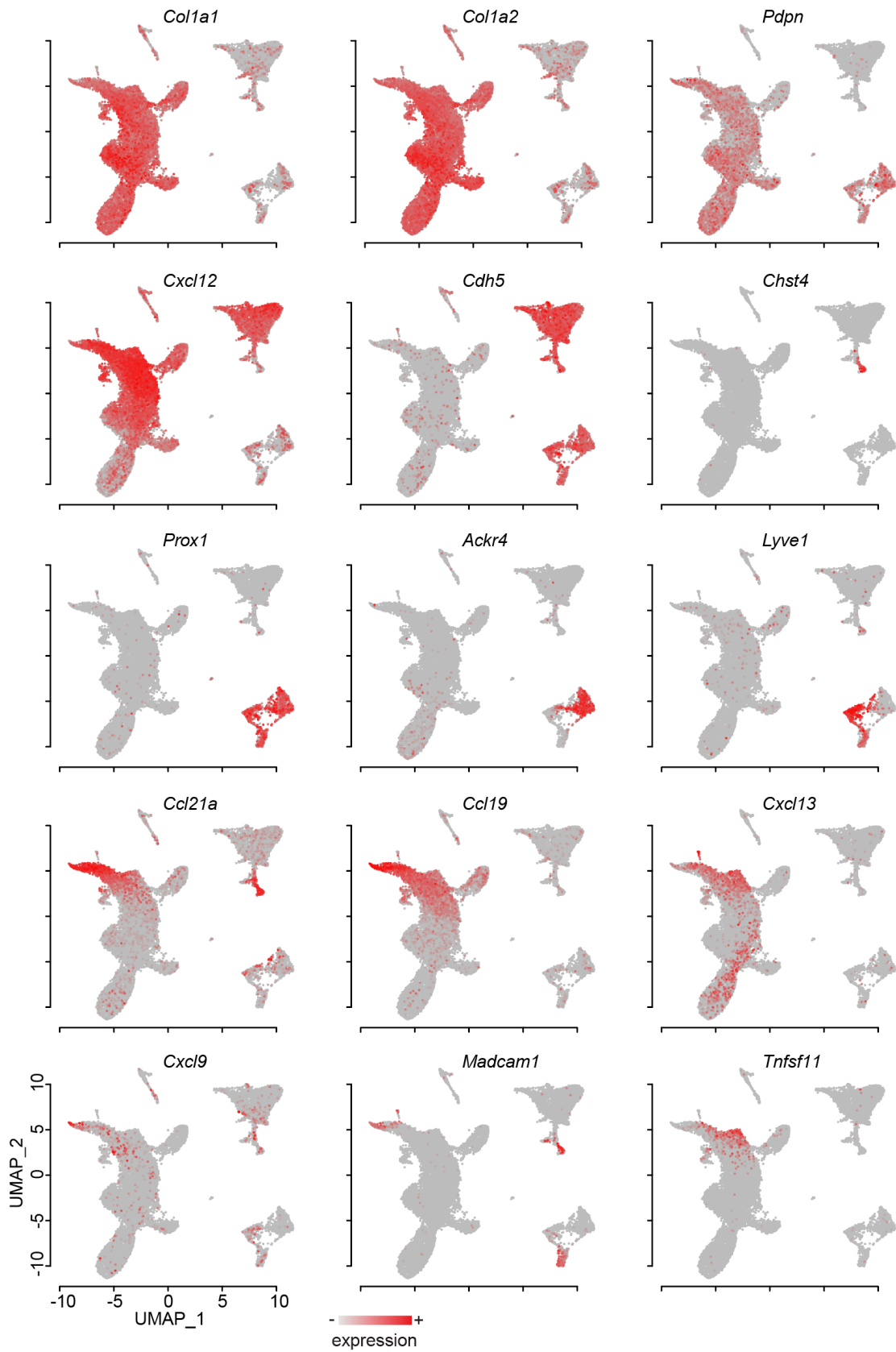


Figure S6

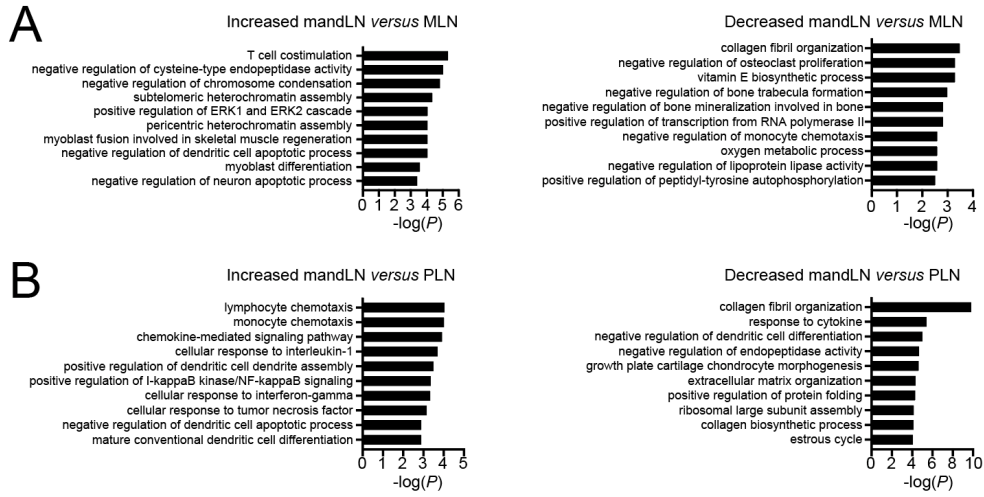


Figure S7

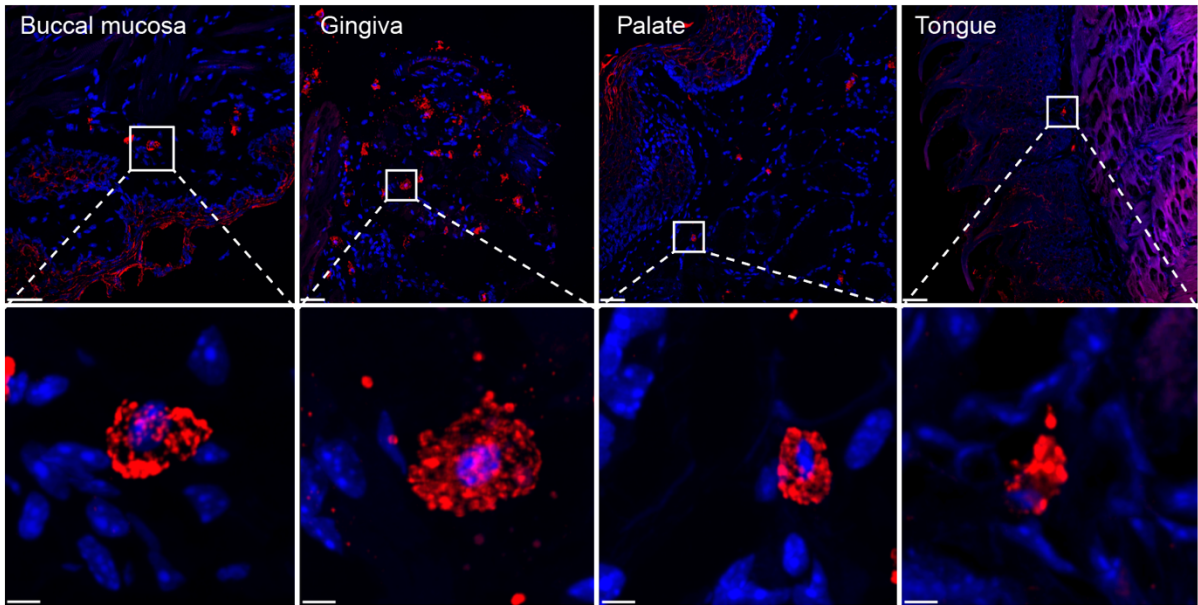


Figure S8